

## The Effect of Fuselage and Rotor Hub on Blade-Vortex Interaction Airloads and Rotor Wakes

Joon W. Lim, Research Scientist (lim@merlin.arc.nasa.gov)  
Aeroflightdynamics Directorate (AMRDEC)  
US Army Research, Development and Engineering Command  
Ames Research Center, Moffett Field, California

Arsenio C. B. Dimanlig, Aerospace Engineer  
Eloret Corp.  
Ames Research Center, Moffett Field, California

The effects of fuselage and hub are studied using coupled computational fluid dynamics (CFD) and computational structural dynamics (CSD) codes to understand their influences on helicopter blade-vortex interaction (BVI) airloads, rotor trim, blade deflections, bending moments, and rotor wakes in descending flight. An iterative loosely-coupled trim methodology was used to couple the OVERFLOW 2 and CAMRAD II codes. Correlations were made for the HART II baseline, minimum noise, and minimum vibration cases at an advance ratio of 0.15, using three levels of modeling — an isolated rotor model, a rotor-hub model, and a rotor-hub/fuselage model. The presence of a rotor hub created strong turbulence, but its effect turned out to be less significant on rotor airloads and trim. The rotor-fuselage model improved the prediction for the phase of  $C_n M^2$  compared to the isolated rotor model, and it also improved the predicted trim controls. This is largely due to more realistic CFD modeling of the onset flow to the rotor due to the presence of fuselage. There was a large difference between the measured data and the predictions for the flap moment, but the predictions for the lead-lag and torsion moments agreed much better with the measured data. Rotor wake positions were predicted with the rotor-fuselage model within approximately one chord length from the measured data for the baseline, minimum noise and minimum vibration cases, and the predictions using the isolated rotor model were as good as the rotor-fuselage model.

### Nomenclature

$C_T$	thrust coefficient
$M$	Mach number
$Q$	2 <sup>nd</sup> order shear of velocity gradient, $s^{-2}$
$R$	blade radius, m
$v$	lead-lag deflection, positive toward the leading edge, m
$w$	flap deflection, positive up, m
$\alpha_s$	shaft angle, positive aft, degrees
$\phi$	elastic torsion, degrees
$\Omega$	rotor operating speed, rad/sec
$\sigma$	solidity
$\theta_0$	collective pitch, degrees
$\theta_{1c}$	lateral cyclic pitch, degrees
$\theta_{1s}$	longitudinal cyclic pitch, degrees
$\mu$	advance ratio
$\psi$	rotor azimuth, degrees

### Introduction

Blade-vortex interaction (BVI) is a significant source of annoying and intrusive noise generated by helicopter rotors. This phenomenon is one of the distinctive features of helicopter rotors, with the noise source becoming especially intrusive during low speed descending and maneuvering flights where the rotor

wake is blown back into the rotor plane. The high noise levels produced by a BVI loading may prohibit rotorcraft from achieving wide acceptance for civil applications.

Over the decades, research efforts to better understand BVI loading and noise have resulted in high-quality measured data available for researchers in this discipline. The HART II test [1-4], which was conducted using a 40% Mach-scaled Bo105 model rotor in the German-Dutch Wind tunnel (DNW), offered a wealth of useful measurements including 3C-PIV (Particle Image Velocimetry), SPR (Stereo Pattern Recognition), noise measurements, and blade pressure. These data are a key resource for investigating the interaction of rotor dynamics, aerodynamics, and rotor wakes.

Recently, many researchers have made efforts for the coupled analysis of computational fluid dynamics (CFD) and computational structural dynamics (CSD) to improve BVI airloads prediction in descending flight [5-13]. These efforts have produced significant improvements in airloads prediction capability from the conventional lifting line theory. More improvement can be made with a physically more complete model that includes a fuselage in the CFD model.

Berry and Bettschart [14] investigated rotor-fuselage interactions using the wind tunnel data of the Dauphin 365N 1/7.7-scaled helicopter model. By correlating with the fuselage pressure data and

comparing between predicted rotor wakes, they identified the need for measured wake data and a computational hub model.

As interest in hub drag reduction has been increased, modeling capability for complex hub structures has significantly improved in CFD models. Using the isolated fuselage and fuselage-hub model, Bridgeman and Lancaster [15] showed correlation with the measured data of the Bell Helicopter light twin airframe wind tunnel test, and demonstrated that hub drag could be accurately predicted using a Navier-Stokes CFD code.

There have been limited numerical studies to investigate the influence of the fuselage for HART II. Kelly et al. [9] applied an unsteady vortex panel method to accurately represent HART II fuselage. Although blade deflections were prescribed with the measured data, the unsteady fuselage effect was not accurately included in the trim computation. More HART II correlation efforts were made by Biedron and Lee-Rausch [12] using FUN3D/CAMRAD II coupled analysis and Boyd [13] using OVERFLOW 2 (ver. 2.1s) / CAMRAD II, and both demonstrated good BVI airloads predictions.

The objective of this paper is to investigate the fuselage effect for HART II by adding rotor hub and fuselage grids to the existing isolated rotor model. The computed results will be compared with the measured data for airloads, trim controls, blade deflections, bending moments and rotor wake positions.

## HART II Computation Model

In descending flight, the flow field below the rotor disk is influenced by interference with the hub/pylon as well as the fuselage. Figure 1 shows computed rotor wake geometries in the baseline case. The wake is represented by iso-surfaces of the 2nd invariant velocity gradient shear tensor, Q-criterion [16, 17], colored with the vorticity magnitude. The fuselage effect is considered primarily as the change in onset flow to the rotor, which affects the rotor loading and wakes, and secondly strong turbulence created behind the hub (near 0 degree azimuth). This effect will be investigated using three different grid models: 1) the isolated rotor, 2) rotor-hub, and 3) rotor-fuselage. Note that the fuselage in the rotor-fuselage grid model includes the hub grid as well as the fuselage grid itself.

### HART II Computation Grids

The HART II rotor [1] is a 40% Mach and dynamically scaled Bo105 hingeless rotor. The rotor blade has a modified NACA 23012 airfoil section with a trailing edge tab 5.4mm long and 0.8mm thick. The blade and cap grids were made using an O-mesh topology. The blade surface grid begins 10cm from the hub center to the blade tip along the span. In the normal direction, the blade near-body grid extends

approximately one chord length from the blade surface. The blade grid system consists of blade grid, root cap and tip cap, and the dimensions of these grids are (295 x 89 x 53), (169 x 49 x 53) and (181 x 81 x 55), respectively. The rotor near-body grids have a total of 10.8 million grid points.

Figure 2 shows HART II fuselage surface grids with a cut through the off-body volume grids. The fuselage grids consist of nine grids/patches including cap grids in the fuselage nose, the end of the sting and the top of the hub cylinder. The near-body grids were made by extending the surface grids to approximately one chord length in the normal direction, and the wall function,  $y^+$  was kept as unity for the first mesh from the surface. The fuselage near-body grids have about 0.7 million grid points. The off-body grids have a level-1 mesh spacing of 0.10 chords near the rotor and fuselage surfaces.

Figure 3 shows the configuration used for this study. The isolated rotor model has 12.1 million grid points for the near-body only, and it has a total of 24.7 million grid points including the near-body and the off-body grids. In the rotor-hub model, hub grid was made by extending the hub cylinder downward to 65cm from the hub center, and it consisted of a total of 27.3 million grid points. The rotor-fuselage grids including the rotor, fuselage, and off-body Cartesian grids have a total of 35.5 million grid points.

### CFD/CSD Analysis

CAMRAD II [18] was used as a CSD tool. The blade was discretized into sixteen nonlinear beam finite elements, with smaller beam elements inboard to capture blade structural behavior. The beam element was represented by three translational (axial, lead-lag, flap) and three corresponding rotational degrees-of-freedom (DOF), resulting in fifteen DOFs for each beam element. The trim was set to satisfy the trim targets (thrust, roll moment and pitching moment) with the trim controls of pitch collective, lateral cyclic, and longitudinal cyclic. A  $15^\circ$  time step was used in the harmonic balance time integration.

An Unsteady Reynolds-Averaged Navier-Stokes code, OVERFLOW 2, was used [19-20] as a CFD tool. The solutions are computed on structured, overset grids having body-conforming near-body grids and Cartesian off-body grids. For time integration, the 1st-order implicit scheme was used with an azimuthal step size of 0.05 degrees (7200 steps per cycle).

For spatial discretization, the 4th-order central differencing has been typically used with the 4th-order artificial dissipation [5, 21] in OVERFLOW 2, resulting in 3rd-order accuracy. The current version of OVERFLOW 2 (version 2.1ae) includes a higher-order Weighted Essentially Non-

**Table 1. Trim controls between the measured data and the computed results using the isolated rotor and rotor-fuselage models in the OVERFLOW 2/CAMRAD II coupled analysis**

	BL			MN			MV		
	Meas.	Rotor	Rotor-fuse	Meas.	Rotor	Rotor-fuse	Meas.	Rotor	Rotor-fuse
$\theta_0$ [deg]	3.80	3.69	3.73	3.91	3.83	3.86	3.80	3.65	3.72
$\theta_{1c}$ [deg]	1.92	1.48	1.75	2.00	1.44	1.72	2.00	1.46	1.75
$\theta_{1s}$ [deg]	-1.34	-0.93	-1.16	-1.35	-0.86	-1.07	-1.51	-0.96	-1.20

Oscillatory (WENO) scheme [22] and its variations. The weighting in the WENO scheme helps to suppress spurious oscillations for relatively smooth solution. Since the 5th-order spatial WENO scheme became 3rd-order accurate at some critical grid points, Henrick et al. [23] developed a mapping technique for the weighting near the critical points in order to maintain the 5th-order accuracy. In this study, the 5th-order Mapped Weighted Essentially Non-Oscillatory (WENOM) scheme was used. The off-body grids used the same order but with an inviscid modeling option for reduced physical dissipation.

A CFD/CSD coupling [5, 12-13, 24-28] is based on the strategy of replacing CSD airloads with CFD airloads, while rotor trim is achieved using CSD to account for blade deformation. The frequency of the airloads information exchange between the CFD and CSD codes is categorized as tight and loose coupling. The former is based on an every time step and the latter is on a per revolution exchange. The present analysis employs the loose coupling strategy.

## Results and Discussion

The effect of the rotor hub and fuselage has been investigated for HART II. Correlations for airloads, blade deformations, bending moments and wake positions are made for the baseline (BL), minimum noise (MN) and minimum vibration (MV) cases.

At the DNW test, the rotor had a shaft tilt of about  $5.3^\circ$  aft, with a thrust level ( $C_T/\sigma$ ) of 0.056 at an advance ratio of 0.15. Since the wind tunnel wall model was not included, the wall-corrected shaft angles in the HART II test report [2] were used for simulation. These were the effective shaft angles corrected by subtracting 0.8-1.2 degrees from the test data — 4.28 degrees for the baseline and 4.12 degrees for the minimum noise and minimum vibration cases. For the isolated rotor and rotor-hub models, the fuselage effect was taken into account by adding 0.2 degrees to the wall-corrected shaft angle.

## Airloads

Figure 4 displays the vorticity maps for the isolated rotor, rotor-hub, and rotor-fuselage models, computed for the baseline case with the reference blade at 0 degree azimuth. The longitudinal cutting planes are shown along the y-axis at  $y/R = -0.7$  (retreating side), 0 (hub center), and 0.7 (advancing side). There appears only small difference in the vorticity map on the advancing and retreating sides between the grids models, but significant difference is seen in the longitudinal plane at the hub center. Although the turbulence created due to the hub might increase the parasite drag significantly, it was not clear how significant these effects were on airloads, trim, structural response, and rotor wakes. Therefore, the effect of rotor hub as well as fuselage is investigated thoroughly.

Figures 5 compares  $C_n M^2$  at  $r/R=0.87$  among the isolated rotor, rotor-hub, and rotor-fuselage models for the baseline, minimum noise and minimum vibration cases. The mean values of  $C_n M^2$  are underpredicted by all three models. It is consistently shown that inclusion of the rotor hub grids does not improve  $C_n M^2$  predictions, but inclusion of the fuselage grids improves the phase of  $C_n M^2$ , especially for the baseline case.

Figure 6 shows the contours of  $C_n M^2$  computed using the isolated rotor, rotor-hub, and rotor-fuselage models for the baseline case. Significant difference of  $C_n M^2$  is shown between the isolated rotor and rotor-fuselage models, while there is a small difference between the isolated rotor and rotor-hub models.

Figures 7-9 compare the harmonic components of  $C_n M^2$  between the isolated rotor and rotor-fuselage models for all three cases. It is seen that the rotor-fuselage model improves the phase of  $C_n M^2$  in both the low frequency (1-6 per-rev) and the mid frequency (7-40 per-rev) BVI modes. The peak-to-peak values of  $C_n M^2$  are slightly improved for the baseline and minimum vibration cases,

while the opposite is seen from the minimum noise case.

The gradients of  $C_n M^2$  are compared in Figs. 10-12 using the isolated rotor and rotor-fuselage models for all three cases. The low-frequency gradients match the measured data well, but the mid-frequency gradients are not as good as the low frequency gradients on the advancing side. This is likely due to numerical difficulties in the BVI loading prediction, which would be caused by diffused old vortices in the first quadrant of the rotor disk or imperfect low-fidelity computation models such as the wind tunnel wall correction.

### Trim

The trim was achieved by setting controls to match the trim targets of measured rotor thrust, roll and pitching moment. The trim controls consist of collective, lateral cyclic and longitudinal cyclic pitches. Figure 13 shows the iteration history of trim controls for the baseline. At each loosely-coupled trim iteration, the reference blade marches a quarter cycles on a periodic basis. The trim controls approach the converged values after several iterations. Since one function evaluation in the CFD analysis was computationally expensive, the number of iterations was taken typically as 8 iterations in earlier studies using OVERFLOW [5, 21].

Figure 14 compares  $C_n M^2$  between the 8th and 12th iteration in the baseline case, and the two computed results are very close to each other, except for the BVI loading on the advancing side. It was shown using an FFT analysis that BVI loading on the advancing side was in the frequency range of 30-40 per-rev while on the retreating side it was in 20-30 per-rev [29]. As seen in the figure, an ability to capture the BVI loading on the advancing side is significantly improved with more trim iterations, and the phase of the 30-40 per-rev BVI loading is in good agreement with the 12th iteration.

The computed trim controls are compared in Fig 15 for the baseline, minimum noise, and minimum vibration cases. Inclusion of the rotor hub grids in OVERFLOW 2 contributes favorably but no significant change to the trim controls. Inclusion of the fuselage grids makes significant improvements for all three cases, which would result from accurately taking into account the change in onset flow to the rotor due to the fuselage. Trimmed controls of the measurements and the

**Table 2. Measured trim targets for the baseline, minimum noise and minimum vibration cases**

	BL	MN	MV
Thrust [N]	3308	3303	3286
Roll mom [Nm]	-15	-31	-16
Pitch mom [Nm]	-25	-30	-29

predictions made using the isolated rotor and rotor-fuselage models are given in Table 1, and the measured trim targets are given in Table 2. Note that the roll moment is defined positive for the right wing up, and the pitching moment is positive for the fuselage nose up.

### Blade Deflections

HART II blade positions and deflections were optically measured using the Stereo Pattern Recognition (SPR) technique [30-31]. The lower side of each black-painted rotor blade, shown in Fig 16, was equipped with 18 reflective markers at the leading edge and another 18 markers at the trailing edge, with each marker having a diameter of 25mm. These markers ranged from  $r/R = 0.228$  to 0.993. For the purpose of hub position identification, four markers — called body markers — were attached underneath the fuselage shell on a rectangular plate. The SPR data were collected for 24 azimuthal locations ( $15^\circ$  increment), with 100 images collected per each azimuthal location.

The measured data adjacent to  $0^\circ$  or  $180^\circ$  azimuth were found damaged due to blocking by the fuselage, or missing where the markers were peeled off from the surface of the blade. To allow smooth blade deformations at radial or azimuthal locations, blade deflection data was synthesized by DLR [32] in the form of a modal representation (3 flap, 2 lead-lag, and 1 torsion modes). The synthesized blade deflection can be reconstructed in terms of the eigenmodes and the generalized coordinates as

$$u(x, \psi) = \sum_j^{N_q} \sum_i^{N_\phi} \Phi(x_i) \cdot q(\psi_j)$$

where the eigenmode,  $\Phi(x_i)$  is formed by the 7th order polynomial for each mode and the generalized coordinate,  $q(\psi_j)$  contains up to 6 per-rev harmonic contents.

The reference blade (blade #1) of the HART II rotor was equipped with 25 newer-type Kulite sensors, which allowed for higher spatial chordwise distribution, while the preceding blade (blade #4) was equipped with 26 older-type Kulite sensors. In fact these two instrumented blades were heavier than the other two uninstrumented blades.

Figures 17-19 show the time histories of blade tip deflections for the baseline, minimum noise, and minimum vibration cases. The measured data depicted as symbols are obtained from the markers on each of four blades, while the computed results shown as lines are obtained from the isolated rotor and rotor-fuselage models. The flap deflection ( $w$ ) at the blade tip is the vertical deflection excluding the vertical height due to a precone angle, and is defined as positive up. The lead-lag deflection ( $v$ )

at the tip is the in-plane deflection, and is positive toward the leading edge. The elastic torsion ( $\phi$ ) is the torsional deflection excluding pitch control and built-in twist, and is positive for the airfoil nose up. The error bound on the deflection measurements was stated as  $\pm 0.5^\circ$  for the elastic torsion and  $\pm 0.5\text{mm}$  for the flap and lead-lag.

For the flap and torsion modes, the measured deflections of all four blades are widely scattered. These scatterings are the blade-to-blade differences, which would result from a tracking problem of the HART II rotor. In the figures, the predicted waveforms match the measured data moderately, and the difference in the predictions between the isolated rotor and rotor-fuselage models seems minimal. It may be noted that scatter of the measured elastic torsion is much larger in the minimum vibration case.

For the lead-lag mode, the blade-to-blade difference seems small, but the predictions show an offset of approximately 1/3 the chord from the measured data. Nonetheless, the predicted waveform matches the measured data well. This discrepancy was not understood but has been commonly found in HART II correlation studies [4, 5]. It is also worth noting that the measured data indicates a lagging motion, while the predicted results show a leading motion, which may result from the inaccurate input of blade structural property near the blade root cutout in the computational model [29].

### Blade Bending Moments

Each blade was equipped identically with six strain gauges. Data acquisition used the sample rate as 256 samples per revolution. The measured bending moment data used in this study was obtained from the reference blade (blade #1).

The blade root cutout is located at  $r/R = 0.22$ , and the inboard region of the root cutout is generally stiffer due to complex structure from blade grip, bolts, bolt holes, pitch horn, etc. Performing correlations of bending moment for this root region is therefore challenging, and it is not unusual to find a large offset in the mean values of blade moment between the measurement and prediction. Thus, we will consider only the oscillatory bending moments (1 per-rev and higher harmonics) in the comparison.

Figures 20-22 compare the oscillatory blade moments between the isolated rotor and rotor-fuselage models for the three cases. For comparison, the blade span location is selected at  $r/R=0.17$  for the flap and lead-lag moments, and the location is at  $r/R=0.33$  for the torsional moment.

For the flap moment, large differences are observed between the measured data and the predictions, but the two predictions using the isolated rotor and rotor-fuselage models are similar to each other for all three cases. For the lead-lag moment, the predicted results are similar to each other like the flap moment, but agree much better with the measured data except for

the discrepancy near the  $180^\circ$  azimuth. The torsional moment predictions match the measured data exceptionally well for the baseline case, though the peak-to-peak values are slightly underpredicted for the minimum noise and minimum vibration cases.

### Rotor Wake Positions

The location and orientation of the PIV measurement windows in the baseline case are shown in Fig. 23. In each PIV measurement plane (black line segment), one hundred instantaneous PIV images were obtained. On the advancing side, the measurement plane orientation angle was preset as  $149.35^\circ$ , and on the retreating side this angle was  $30.06^\circ$ . As shown in the figure, PIV measurements were taken in the 2nd and 4th quadrants when the reference blade was at  $70^\circ$  azimuth, and were taken in the 1st and 3rd quadrants when it was at  $20^\circ$ . The vortices found in the 2nd quadrant (positions 17-19) and the 3rd quadrant (positions 43-45) were relatively young vortices, while those in the 1st quadrant (positions 20-23) and the 4th quadrant (positions 46-47) were older vortices.

Figure 24 shows the iso-surfaces of Q-criterion for the baseline case with the reference blade at an azimuth of  $20^\circ$ , colored by the vorticity magnitude with red indicating high strength. Several discrete tip vortices, shown on the retreating side, travel to the advancing side and get diffused. In the rear side of the rotor, strong turbulence is created from interference with the rotor hub. The coordinate surfaces in the figure show the longitudinal cutting planes at  $y/R = \pm 0.7$ , where the wake measurements were made. The visualized rotor wake image shows significant details of the rotor wakes, despite the fact that the computational mesh size is not nearly as fine as needed.

Rotor wake positions in the longitudinal cutting planes at  $y/R = \pm 0.7$  are compared in Fig. 25 for the baseline case. The wake positions upstream of the hub are well predicted within a deviation of approximately one chord for both the advancing and retreating sides. It is worth noting that the predictions using the isolated rotor model are as good as the rotor-fuselage model.

At some measurement positions, identifying wake positions was extremely difficult partly due to diffused tip vortices with age and the interactions between blade-to-vortex, vortex-to-vortex, or shear layer-to-vortex. As an example, Fig. 26 shows the rotor wake field adjacent to the PIV measurement position 23, computed using the rotor-fuselage model. The vortex of interest is the one that was initiated from the reference blade at an azimuth of  $135.6^\circ$  and then reached position 23 with an age of  $515.3^\circ$ . In the neighborhood of this vortex, another vortex is found that was initiated from blade #3 at an azimuth of  $44.4^\circ$  and traveled to this position

with an age of  $66.5^\circ$ . These two vortices were almost collocated with their strengths opposite to each other. Since the other vortex is young and strong, and also these two vortices interact with a shear layer, identifying this vortex of interest was not as straightforward as one would hope.

Figure 27 compares the wake positions for the minimum noise case. Note that the measurement was missed for position 23. Similar to the baseline case, the predicted positions correlate well with the measured data both on the advancing and retreating sides.

Figure 28 shows the iso-surfaces of Q-criterion for the minimum vibration case with the reference blade at an azimuth of  $20^\circ$  and the vorticity map at  $y/R = 0.7$  depicting the vortices for positions 19-22 and 20v-23v. The rotor wake field looks much more complex due to presence of the dual tip vortices on the advancing side. These dual vortices resulted from a negative tip loading on the advancing side. The primary tip vortex has a negative strength (counter-rotating) and convects downstream from the blade tip, while the secondary tip vortex that was initiated slightly inboard from the tip has a positive vortex strength (rotating) and appears stronger than the primary vortex. Vorticity map shown is the coordinate surface at  $y/R = 0.7$  where the vortices in positions 19-22 and 20v-23v are found.

Figure 29 shows the wake positions for the minimum vibration case. On the advancing side, the counter-rotating vortices are for positions 53 and 18v-23v, and the rotating ones are for positions 18-22. On the retreating side, rotating, single tip vortices travel along the vortex trajectory. The predicted wake positions on the advancing and retreating sides correlate well with the measured data. Note that the measurement of the rotating vortex at position 17 was missed during the test.

### CPU Time

The computational resource used for this study was an Altix 4700 based, NASA Advanced Supercomputing (NAS) Columbia system assembled with Intel Itanium 9000 series 1.6 GHz processors, having 512-1024 dual cores.

Table 3 compares the total grid points and OVERFLOW 2 CPU time used between the isolated rotor and rotor-fuselage models. Both runs were made using 64 processors. The CPU time is measured by "Proc-hours" which is defined as the number of processors times the CPU time (hours) required for one full revolution (= 7200 time steps). When fuselage grids were added to the isolated rotor grids, total grid points were increased by 44%. So, a 65% increase in the CPU time with the rotor-fuselage model seems largely due to the increase in the number of grid points.

### Concluding Remarks

Coupling of unsteady and three-dimensional OVERFLOW 2 CFD aerodynamics solutions into the

**Table 3. Comparison of OVERFLOW 2 CPU time required for one full revolution between the isolated rotor and rotor-fuselage models**

	Rotor	Rotor-fuse	% increase
Grids (million pts.)	24.7	35.5	44
Proc-hours	837	1379	65

CAMRAD II code has improved the capability of rotor airloads prediction in descending flight. Although inclusion of fuselage grids adds complexity, OVERFLOW 2 was capable of displaying an overall improvement for airloads prediction over the isolated rotor model.

In addition to these general observations, the following conclusions are drawn from the results presented:

1) Presence of the rotor hub created strong turbulence due to interference with the hub cylinder, which might increase the parasite drag significantly compared to the isolated rotor model, but its effect turned out to be less significant on rotor airloads and trim.

2) The rotor-fuselage model improved the phase of  $C_n M^2$  in both the low frequency (1-6 per-rev) mode and the mid frequency (7-40 per-rev) BVI mode, compared to the isolated rotor model.

3) The rotor-fuselage model improved trim controls for all three cases compared to the isolated rotor model, which would result from accurately taking into account the change in onset flow to the rotor due to the fuselage.

4) The waveforms of flap, lead-lag and elastic torsion deflections were moderately predicted using the isolated rotor and rotor-fuselage models. The two predictions were close to each other.

5) For flap moment, large differences between the measured data and the predictions were observed. The predictions for lead-lag and torsion moments agreed much better with the measured data. The predicted flap, lead-lag and torsion moments using both the isolated rotor and rotor-fuselage models were close to each other for the baseline, minimum noise, and minimum vibration cases.

6) Rotor wake positions with the rotor-fuselage model were predicted within approximately one chord length from the measured data for the baseline, minimum noise, and minimum vibration cases. The predictions using the isolated rotor model were as good as the rotor-fuselage model.

7) An increase in the CPU time with the rotor-fuselage model seems largely due to the increase in the number of grid points.

## Acknowledgements

The authors would like to acknowledge the support of HART II partners — DLR, DNW, NASA, ONERA and AFDD. The authors also would like to thank Dr. David D. Boyd, Jr., NASA Langley Research Center for invaluable discussion about the OVERFLOW 2 WENOM scheme, and Mr. Mark Potsdam, US Army AFDD for discussion on fuselage modeling in OVERFLOW 2.

## References

- <sup>1</sup>Yu, Y. H., Tung, C., van der Wall, B. G., Pausder, H., Burley, C., Brooks, T., Beaumier, P., Delrieux, Y., Mercker, E., and Pengel, K., “The HART-II Test: Rotor Wakes and Aeroacoustics with Higher-Harmonic Pitch Control (HHC) Inputs-The Joint German/French/Dutch/US Project,” American Helicopter Society 58th Annual Forum Proceedings, Montreal, Canada, June 11-13, 2002.
- <sup>2</sup>van der Wall, B. G., “2nd HHC Aeroacoustics Rotor Test (HART II) – Part I: Test Documentation,” DLR IB 111-2003/19, Braunschweig, Germany, November 2003.
- <sup>3</sup>Burley, C. L., Brooks, T. F., van der Wall, B., Richard, H., Raffel, M., Beaumier, P., Lim, J., Yu, Y.H., Tung, C., and Pengel, K., “Rotor Wake Vortex Definition and Validation from 3-C PIV HART-II Study,” 28th European Rotorcraft Forum Proceedings, Bristol, England, September 2002.
- <sup>4</sup>Lim, J. W., Tung, C., Yu, Y. H., Burley, C. L., Brooks, T. F., Boyd, D., van der Wall, B. G., Schneider, O., Richard, H., Raffel, M., Beaumier, P., Delrieux, Y., Pengel, K., and Mercker, E., “HART II: Prediction of Blade-Vortex Interaction Loading,” 29th European Rotorcraft Forum Proceedings, Friedrichshafen, Germany, September 16-18, 2003.
- <sup>5</sup>Lim, J., Nygaard, T. A., Strawn, R., and Potsdam, M., “Blade-Vortex Interaction Airloads Prediction Using Coupled Computational Fluid and Structural Dynamics,” *Journal of the American Helicopter Society*, Vol. 52, (4), October 2007, pp. 318-328.
- <sup>6</sup>Lim, J. W., and Strawn, R. C., “Prediction of HART II Rotor BVI Loading and Wake System Using CFD/CSD Loose Coupling,” *Journal of Aircraft*, Vol. 45, (3), May-June, 2008, pp. 923-933.
- <sup>7</sup>Dietz, M., Kramer, E., and Wagner, S., “Tip vortex conservation on a main rotor in slow descent flight using vortex-adapted Chimera grids,” 24th AIAA Applied Aerodynamics Conference Proceedings, Paper No AIAA-2006-3478, San Francisco, CA, June 2006.
- <sup>8</sup>Yang, C., Inada, Y., and Aoyama, T., “BVI Noise Prediction Using HART II Motion Data,” International Forum of Rotorcraft Multidisciplinary Technology Proceedings, Seoul, Korea, October 2007.
- <sup>9</sup>Kelly, M. E. and Brown, R. E., “The Effect of Blade Aerodynamic Modelling on the Prediction of High Frequency Rotor Airloads,” American Helicopter Society 65th Annual Forum Proceedings, Grapevine, Texas, 2009.
- <sup>10</sup>Renaud, T., Perez, G., Benoit, C., Jeanfaivre, G., and Peron, S., “Blade-Vortex Interaction Capture by CFD,” 34th European Rotorcraft Forum Proceedings, Liverpool, England, September 16-19, 2008.
- <sup>11</sup>Lee, H., Kwak, J., Shin, S. J., Yang, C., and Aoyama, T., “Aerodynamic / Structural / Acoustic Prediction of HART II Rotor Using Weakly Coupled CFD-CSD Analysis,” American Helicopter Society 65th Annual Forum Proceedings, Grapevine, Texas, 2009.
- <sup>12</sup>Biedron, R. T., and Lee-Rausch, E. M., “Rotor Airloads Prediction Using Unstructured Meshes and Loose CFD/CSD Coupling,” 26th AIAA Applied Aerodynamics Conference, AIAA Paper 2008-7341, Honolulu, Hawaii, August 18-21, 2008.
- <sup>13</sup>Boyd, D. D., “HART-II Acoustic Predictions using a Coupled CFD/CSD Method,” American Helicopter Society 65th Annual Forum Proceedings, Grapevine, Texas, May 27-29, 2009.
- <sup>14</sup>Berry, J., and Bettschart, N., “Rotor-Fuselage Interaction: Analysis and Validation with Experiment,” American Helicopter Society 53rd Annual Forum Proceedings, Virginia Beach, Virginia, April 29-May 1, 1997.
- <sup>15</sup>Bridgeman, J. O., and Lancaster, G. T., “Physics-based Analysis methodology for Hub Drag Prediction,” American Helicopter Society 66th Annual Forum Proceedings, Phoenix, Arizona, May 11-13, 2010.
- <sup>16</sup>Jeong, J., and Hussain, F., “On the Identification of a Vortex,” *Journal of Fluid Mechanics*, Vol. 285, 1995, pp. 69-94.

<sup>17</sup>van der Wall, B. G., and Richard, H., "Analysis Methodology for 3C PIV Data," 31st European Rotorcraft Forum, Florence, Italy, September 2005.

<sup>18</sup>Johnson, W., "Influence of Wake Models on Calculated Tiltrotor Aerodynamics," American Helicopter Society Aerodynamics, Acoustics, and testing and Evaluation Technical Specialists Meeting Proceedings, San Francisco, CA, January 2002.

<sup>19</sup>Buning, P., "Consolidation of Time-Accurate, Moving Body Capabilities in OVERFLOW," 6th Overset Composite Grid and Solution Technology Symposium Proceedings, Ft. Walton Beach, Florida, October 8-10, 2002.

<sup>20</sup>Buning, P., G., Gomez, R. J., and Scallion, W. I., "CFD Approaches for Simulation of Wing-Body Stage Separation," AIAA 2004-4838, 22nd AIAA Applied Aerodynamics Conference Proceedings, Providence, RI, August 2004.

<sup>21</sup>Potsdam, M., Yeo, H., and Johnson, W., "Rotor Airloads Prediction Using Loose Aerodynamic/Structural Coupling," *Journal of Aircraft*, Vol. 43, (3), May-June, 2006, pp. 732-742.

<sup>22</sup>Nichols, R. H., Tramel, R. W., Buning, P. G., "Evaluation of Two High-Order Weighted Essentially Nonoscillatory Schemes," *AIAA Journal*, Vol. 46, No. 12, December 2008, pp. 3090-3102.

<sup>23</sup>Henrick, A., Aslam, T., and Powers, J., "Mapped Weighted Essentially Non-Oscillatory Schemes: Achieving Optimal Order Near Critical Points," *Journal of Computational Physics*, Vol. 207, August 2005, pp. 542-567.

<sup>24</sup>Tung, C., Caradonna, F. X., and Johnson, W. R., "The Prediction of Transonic Flows on an Advancing Rotor," American Helicopter Society 40th Annual Forum Proceedings, Arlington, Virginia, May 1984.

<sup>25</sup>Servera, G., Beaumier, P., and Costes, M., "A Weak Coupling Method Between the Dynamics Code HOST and the 3D Unsteady Euler Code WAVES," 26th European Rotorcraft Forum Proceedings, The Hague, Netherlands, September 2000.

<sup>26</sup>Pahlke, K. and Van Der Wall, B., "Chimera simulations of multibladed rotors in high-speed forward flight with weak fluid-structure-coupling," *Aerospace Science and Technology*, Vol. 9, (5), 2005, pp. 379-389.

<sup>27</sup>Datta, A., Sitaraman, J., Chopra, I., and Baeder, J. D., "CFD/CSD prediction of Rotor Vibratory Loads in High-Speed Flight," *Journal of Aircraft*, Vol. 43, (6), November-December 2006, pp. 1698-1709.

<sup>28</sup>Min, B. Y., Sankar, L., Prasad, J., and Schrage, D., "A Physics-Based Investigation of Gurney Flaps for Rotor Vibration Reduction," American Helicopter Society 65th Annual Forum Proceedings, Grapevine, Texas, May 27-29, 2009.

<sup>29</sup>Lim, J. W., "An Assessment of Rotor Dynamics Correlation for Descending Flight Using CFD/CSD Coupled Analysis," American Helicopter Society 64th Annual Forum Proceedings, Montreal, Canada, April 29-May 1, 2008.

<sup>30</sup>Pengel, K., Mueller, R., van der Wall, B.G., "Stereo Pattern Recognition – the technique for reliable rotor blade deformation and twist measurement," Heli-Japan 2002, AHS International Meeting on Advanced Rotorcraft Technology and Life Saving Activities Proceedings, Utsunomiya, Japan, November 2002.

<sup>31</sup>Schneider, O., "Analysis of SPR Measurements from HART II," *Aerospace Science and Technology*, Vol. 9, (5), 2005, pp. 409-420.

<sup>32</sup>van der Wall, B. G., "Mode identification and data synthesis of HART II blade deflection data," DLR IB 111-2007/28, Braunschweig, Germany, June 2007.

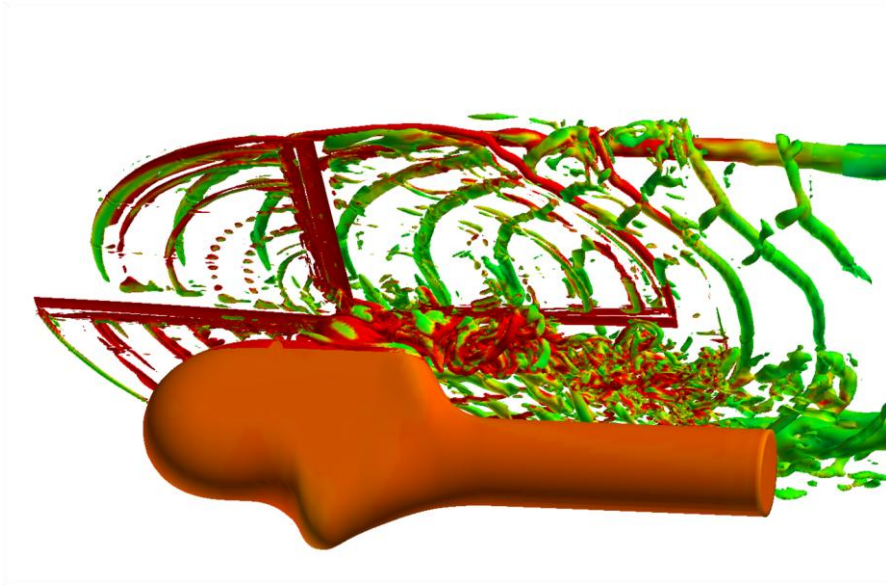


Figure 1. Computed rotor wake geometries by Q-criterion for the baseline case (reference blade at 0 degrees).

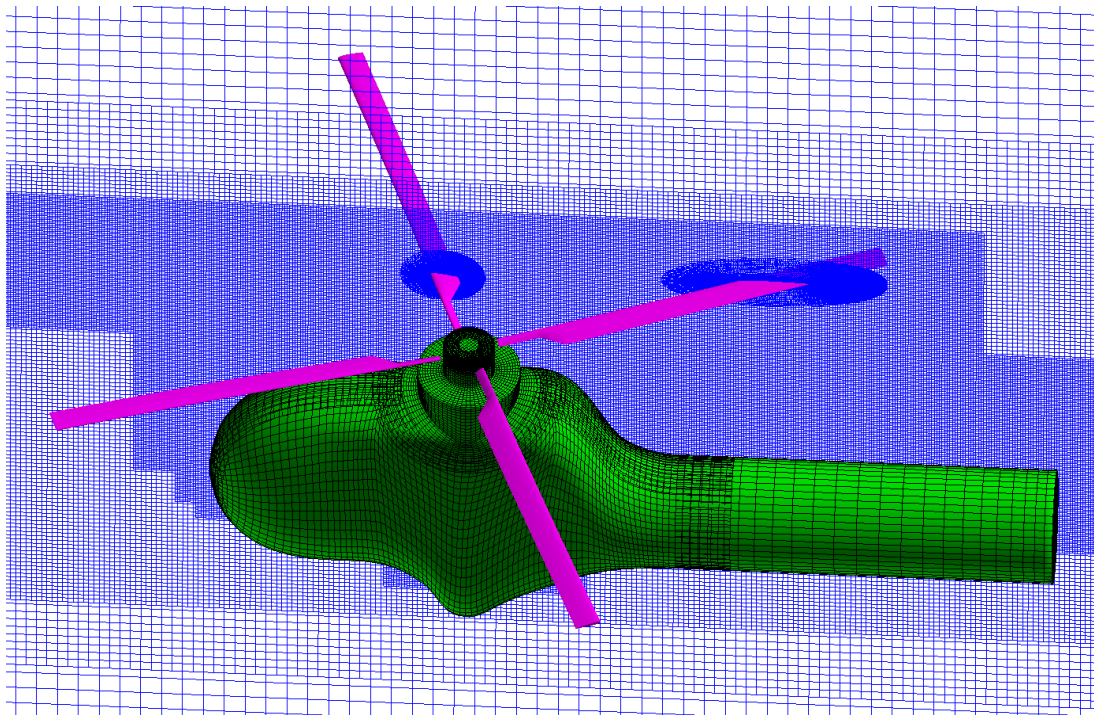


Figure 2. HART II fuselage surface grids with a cut through the off-body volume grids.

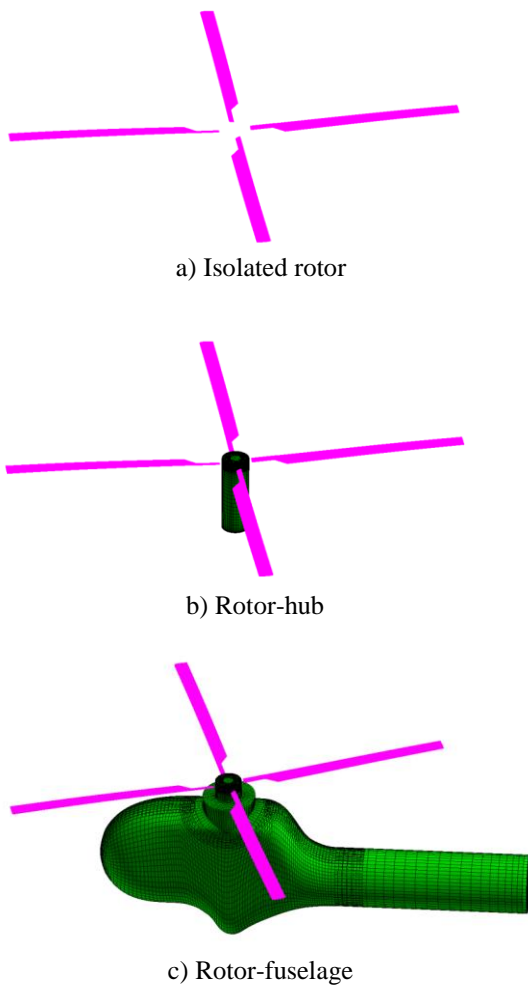


Figure 3. Three different CFD surface grids nodes: a) the isolated rotor, b) the rotor-hub, and c) the rotor-fuselage.

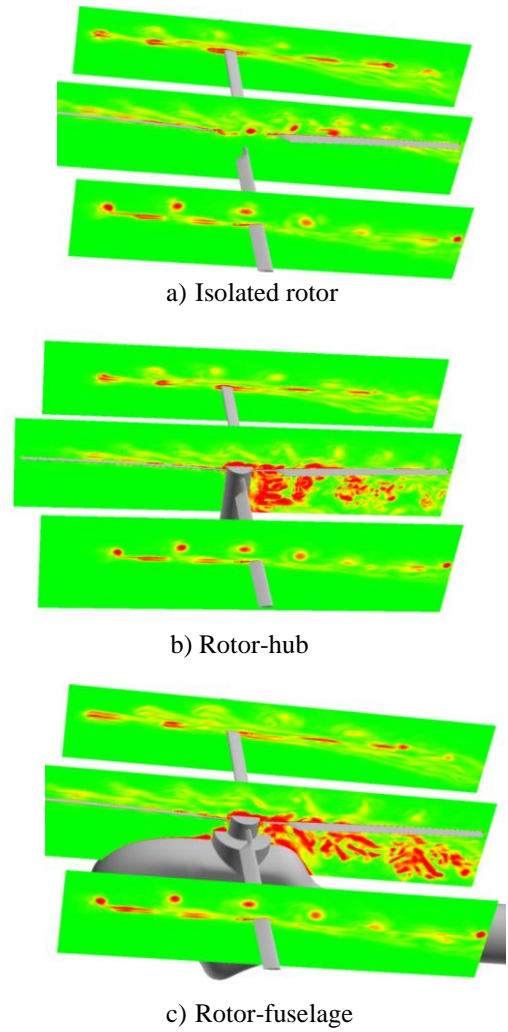
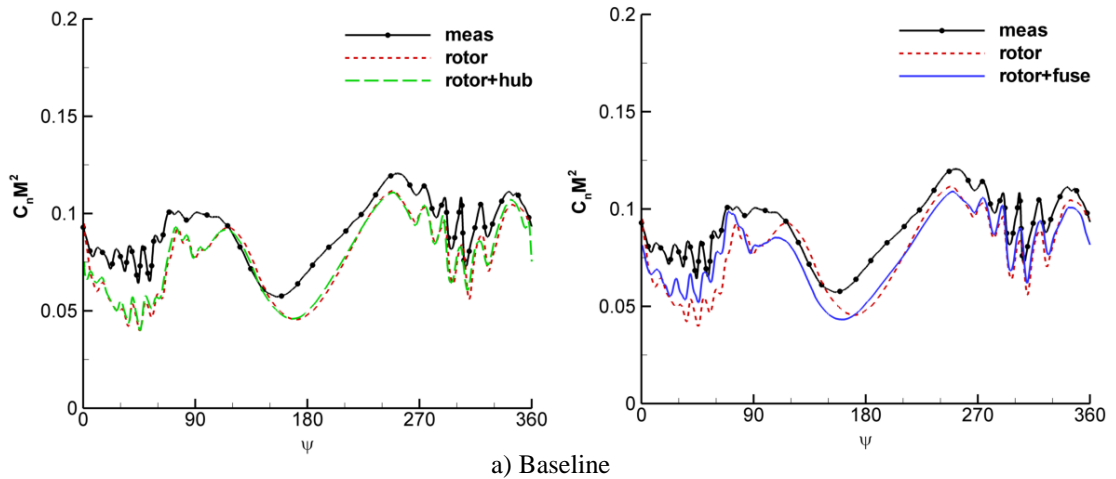
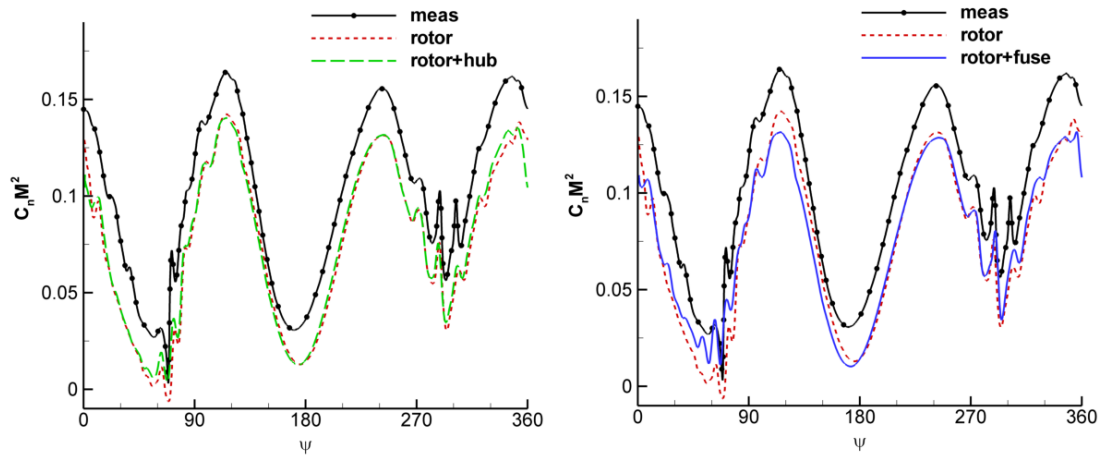


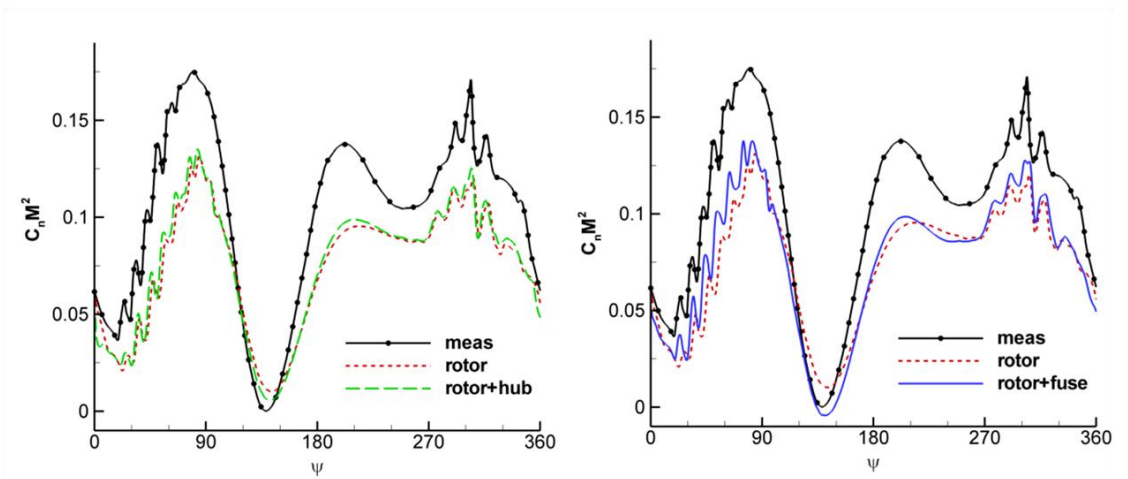
Figure 4. Vorticity maps at  $y/R=0, \pm 0.7$  using three different CFD grids for the baseline case with the reference blade at 0 degree azimuth.



a) Baseline



b) Minimum noise



c) Minimum vibration

Figure 5. Comparison of  $C_n M^2$  at  $r/R=0.87$  using the isolated rotor, rotor-hub and rotor-fuselage models for the baseline, minimum noise, and minimum vibration cases.

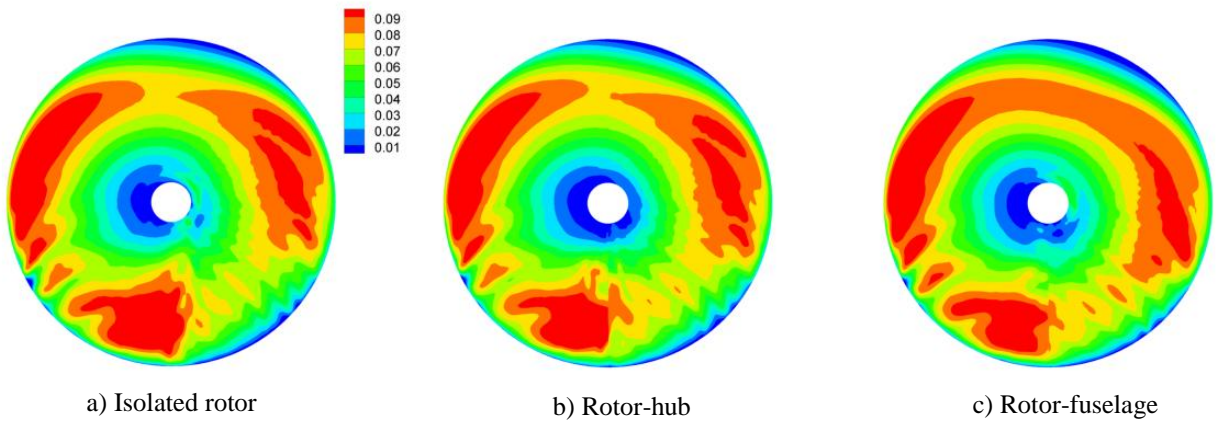
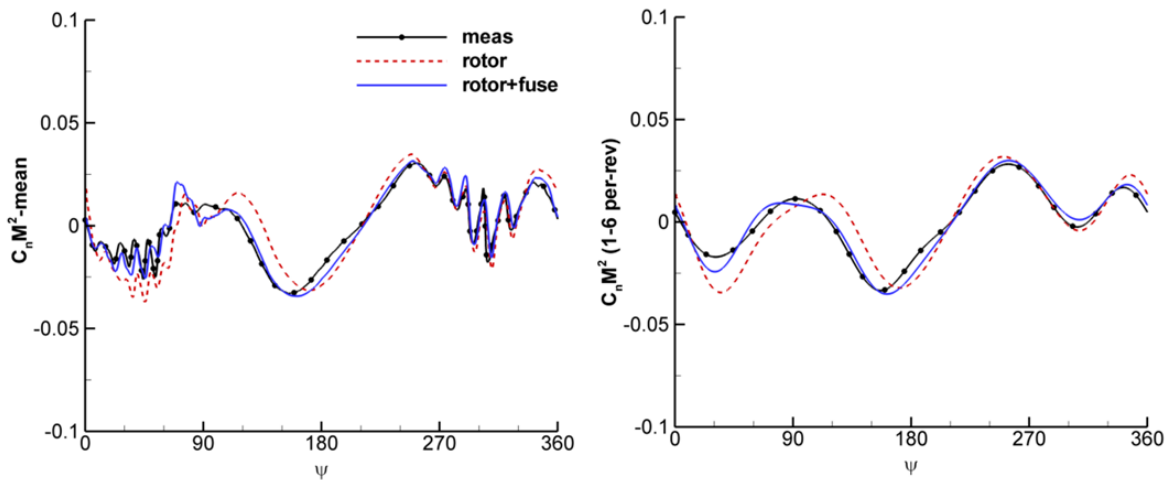
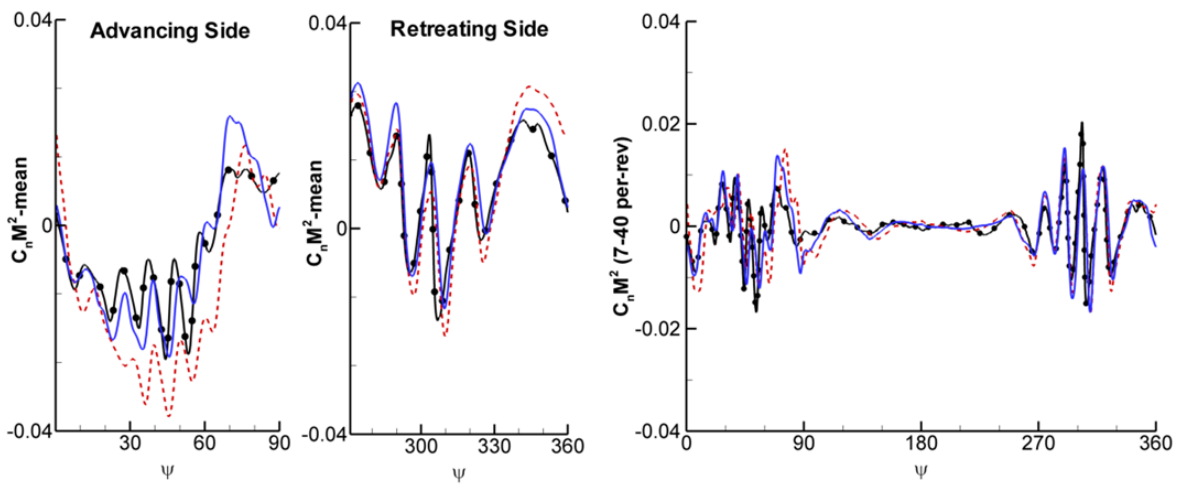


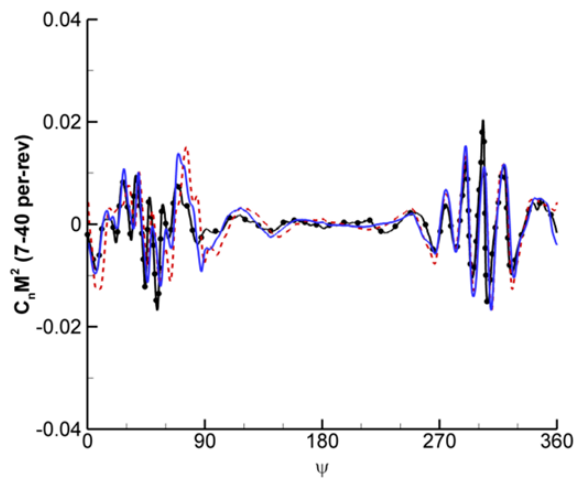
Figure 6. Comparison of the contours of  $C_n M^2$  computed using the isolated rotor, rotor-hub and rotor-fuselage models for the baseline case.



a) Low frequency (1-6 per-rev)



a) Mean removed



c) Mid frequency (7-40 per-rev)

Figure 7. Comparison of the harmonic components of  $C_n M^2$  at  $r/R=0.87$  using the isolated rotor, rotor-hub, and rotor-fuselage models for the baseline case.

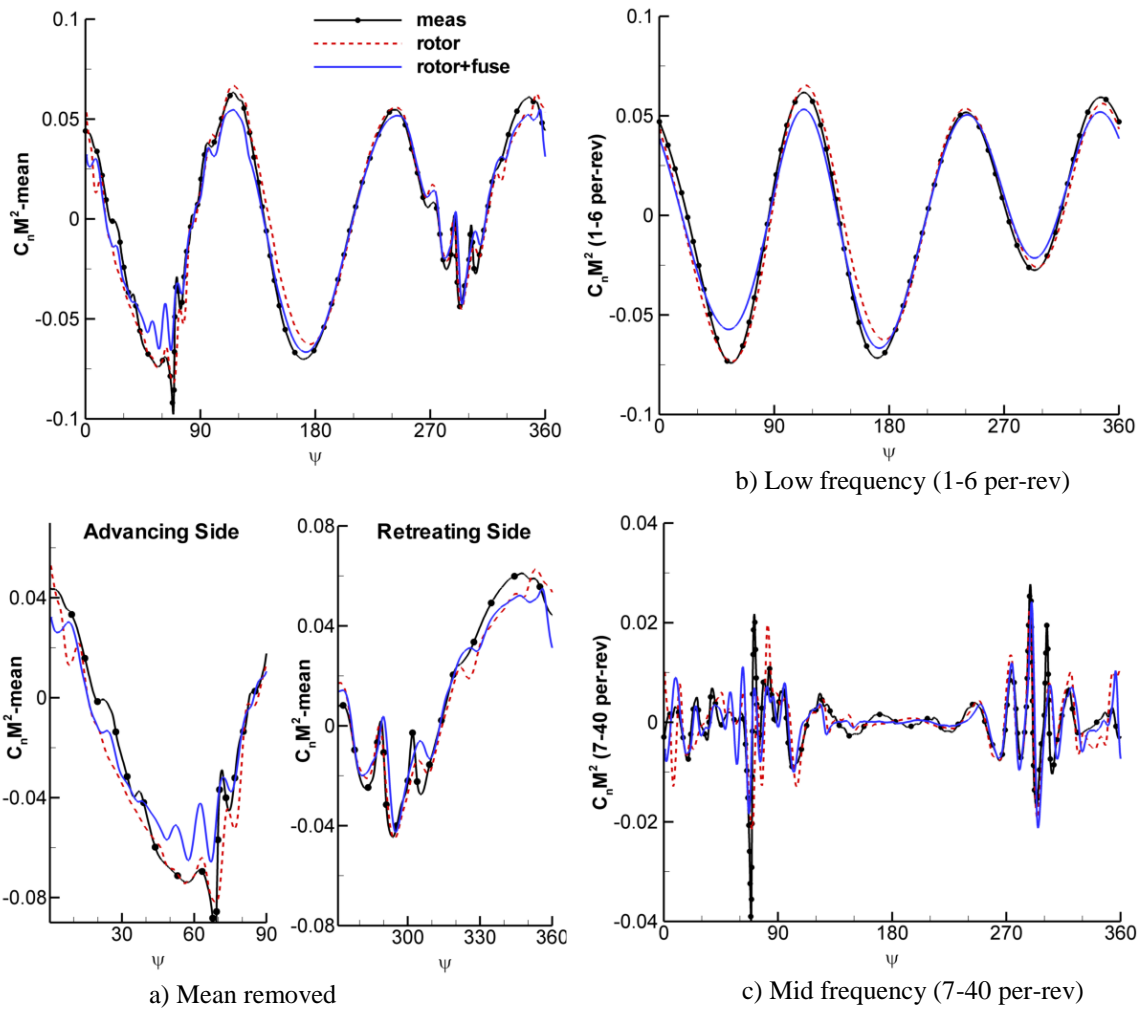


Figure 8. Comparison of the harmonic components of  $C_n M^2$  at  $r/R=0.87$  using the isolated rotor, rotor-hub, and rotor-fuselage models for the minimum noise case.

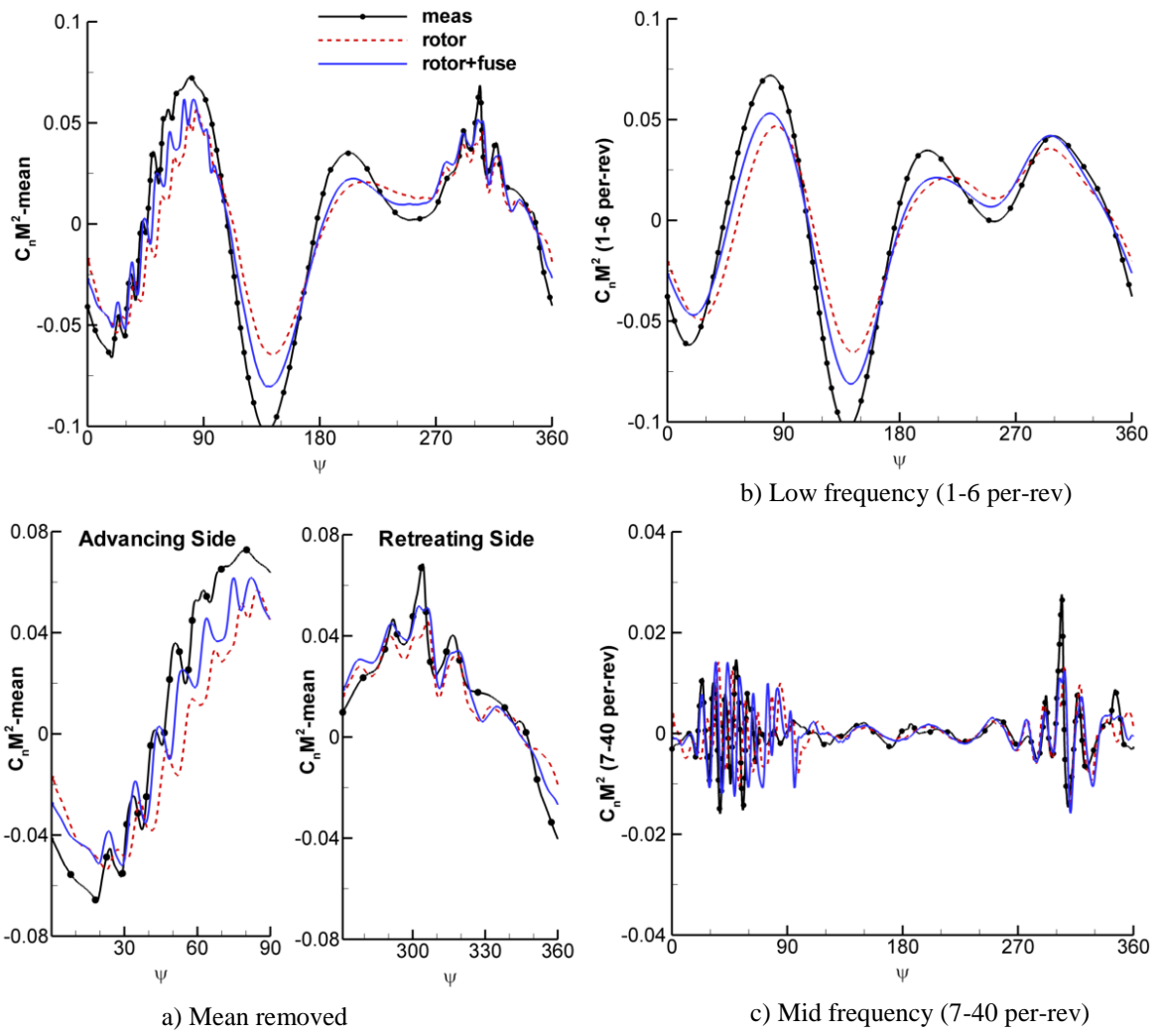
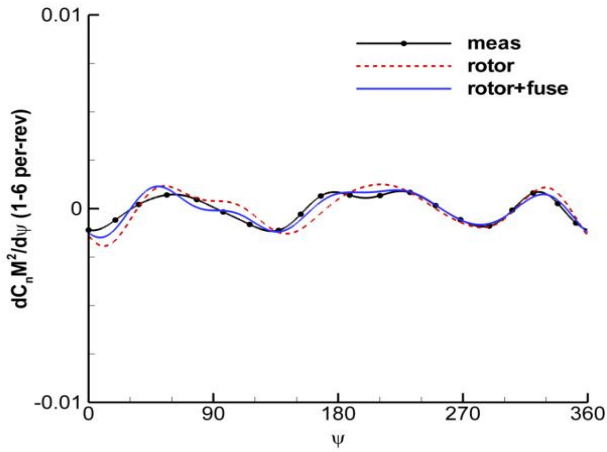
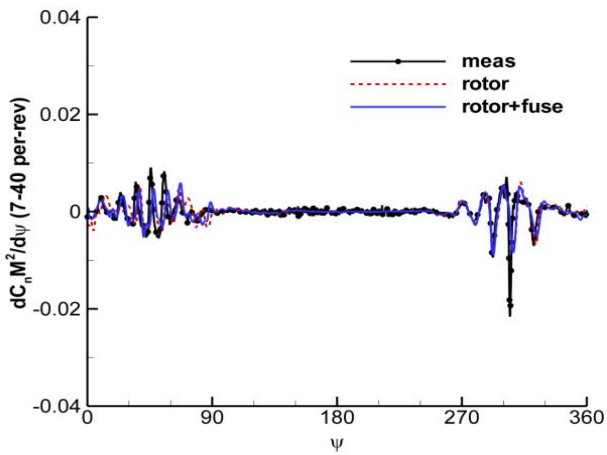


Figure 9. Comparison of the harmonic components of  $C_n M^2$  at  $r/R=0.87$  using the isolated rotor, rotor-hub, and rotor-fuselage models for the minimum vibration case.



a) Low frequency (1-6 per-rev)



b) Mid frequency (7-40 per-rev)

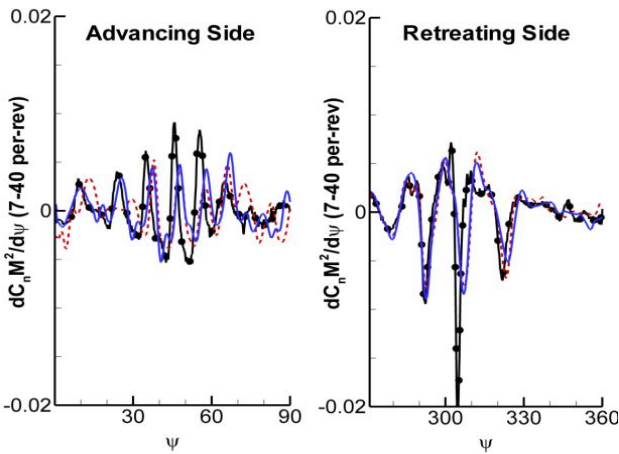
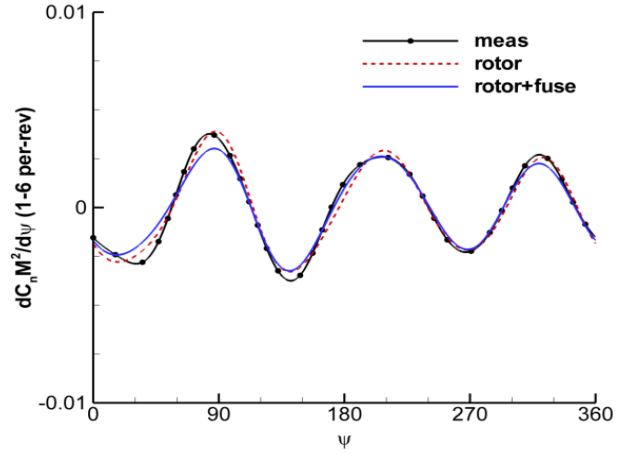
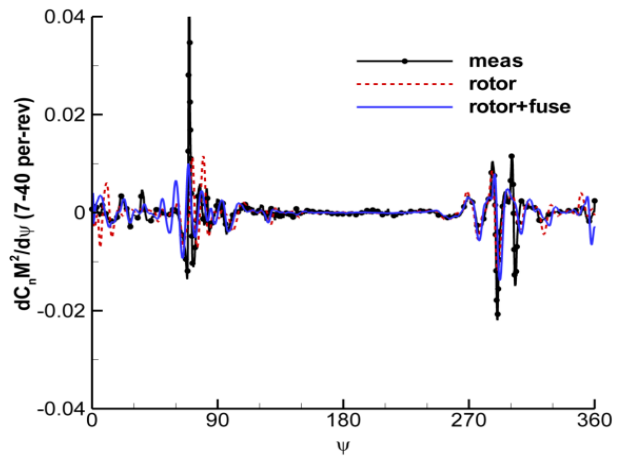


Figure 10. Comparison of the gradient of the harmonic  $C_n M^2$  at  $r/R=0.87$  using the isolated rotor and rotor-fuselage models for the baseline case.



a) Low frequency (1-6 per-rev)



b) Mid frequency (7-40 per-rev)

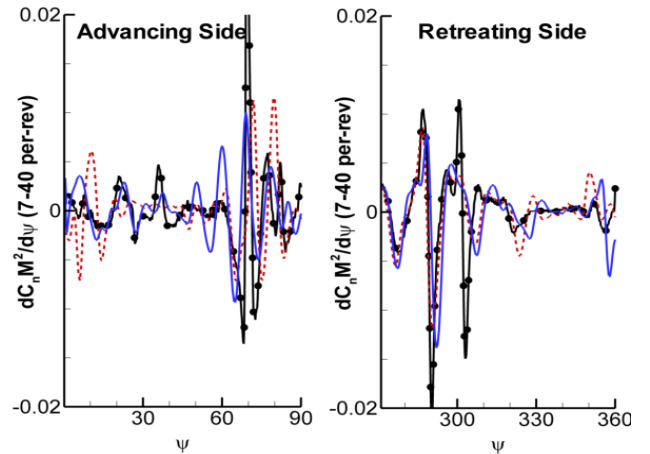
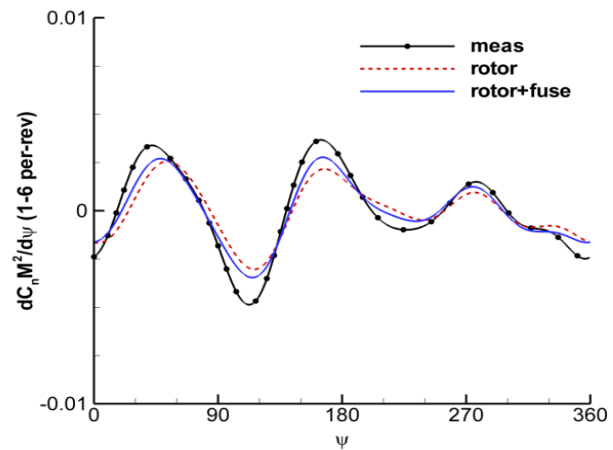
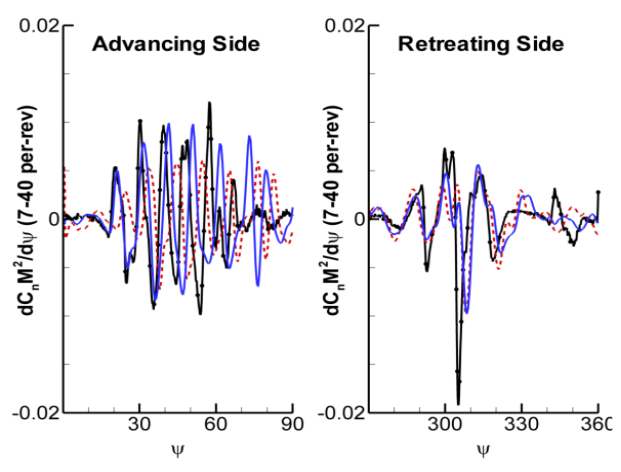
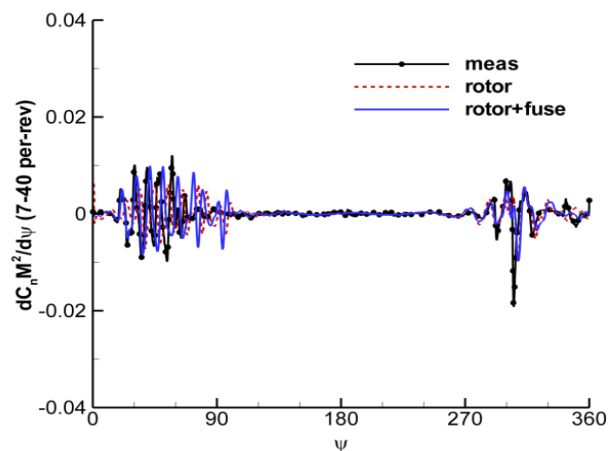


Figure 11. Comparison of the gradient of the harmonic  $C_n M^2$  at  $r/R=0.87$  using the isolated rotor and rotor-fuselage models for the minimum noise case.



a) Low frequency (1-6 per-rev)



b) Mid frequency (7-40 per-rev)

Figure 12. Comparison of the gradient of the harmonic  $C_n M^2$  at  $r/R=0.87$  using the isolated rotor and rotor-fuselage models for the minimum vibration case.

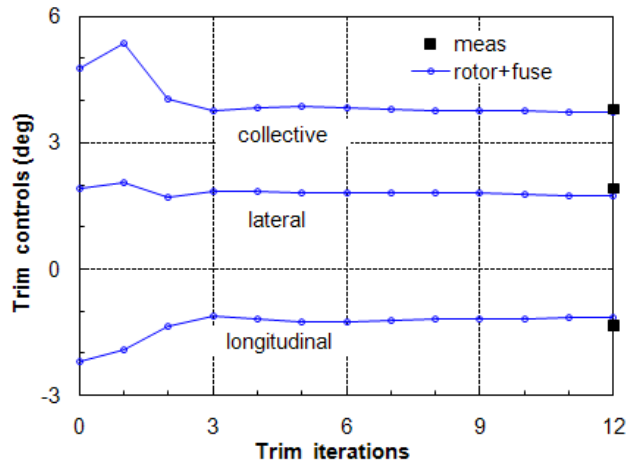


Figure 13. Iteration history of trim controls using the rotor-fuselage model for the baseline case.

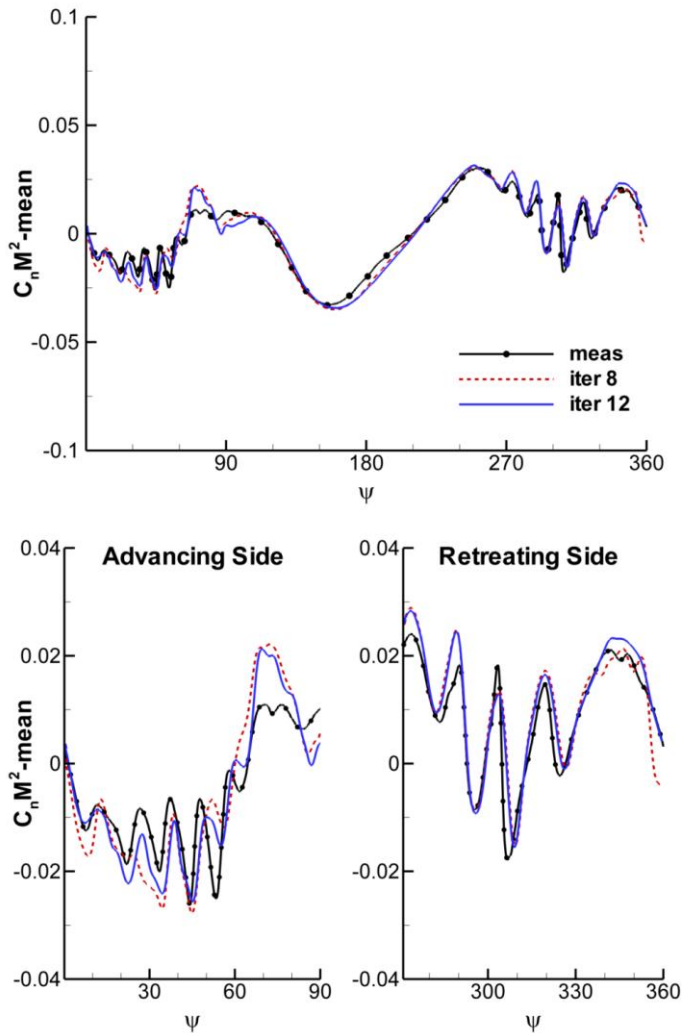


Figure 14. Comparison of  $C_n M^2$  at  $r/R=0.87$  between iteration #8 and #12 using the rotor-fuselage model in the minimum vibration case.

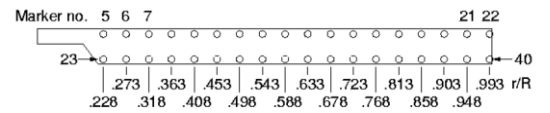
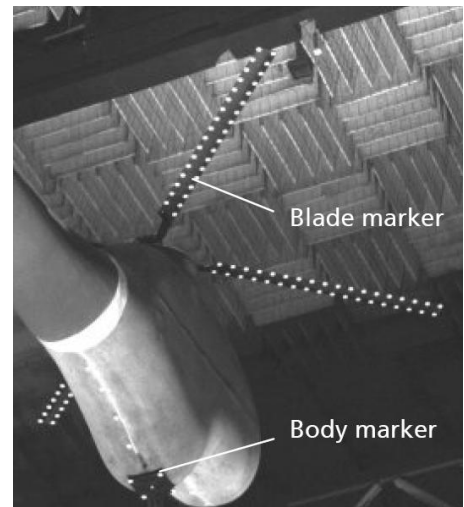
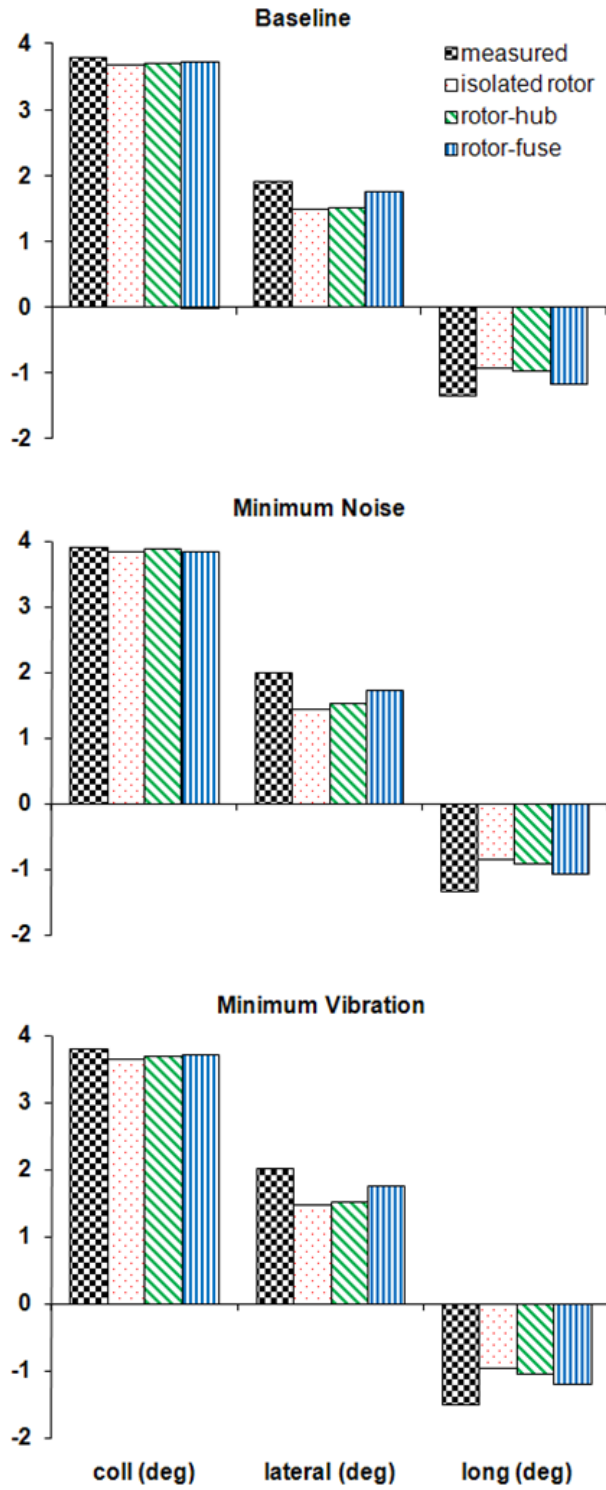


Figure 16. SPR images from the rear right camera with the reference blade at an azimuth of 135° [2].

Figure 15. Computed trim controls using the isolated rotor, rotor-hub, and rotor-fuselage models for the baseline, minimum noise, and minimum vibration cases.

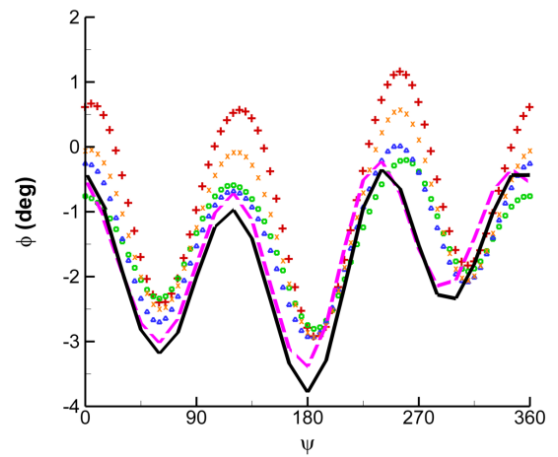
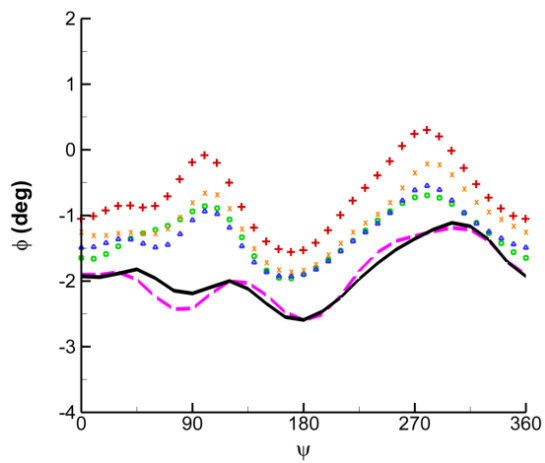
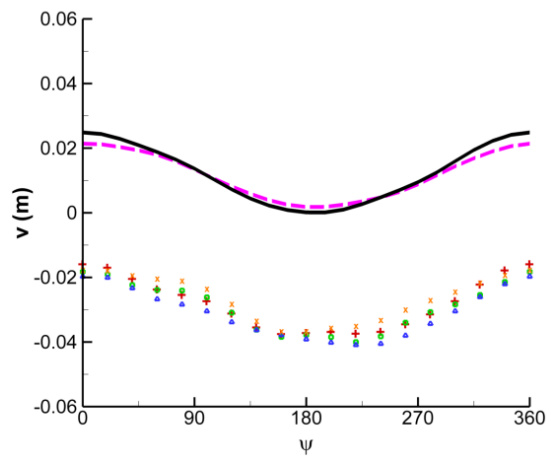
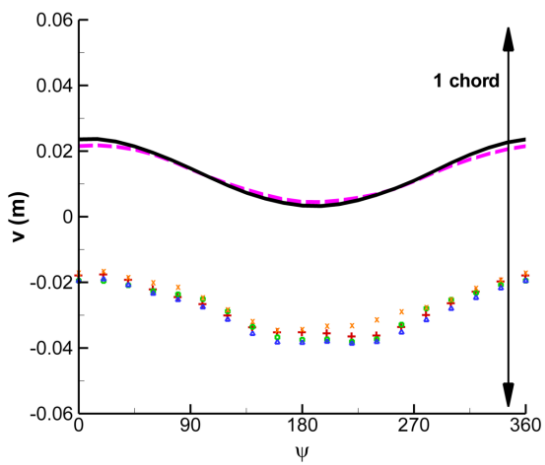
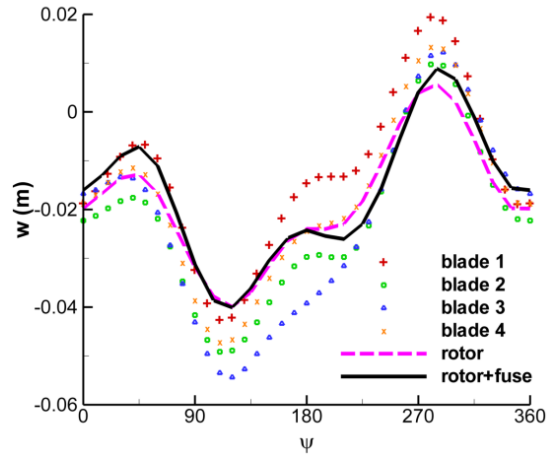
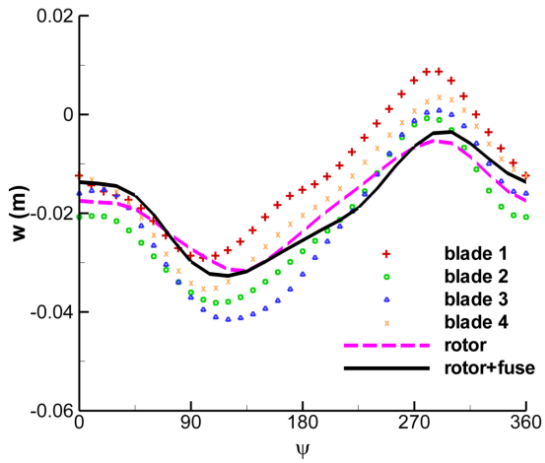


Figure 17. Blade tip deflections (flap, lead-lag and elastic torsion) measured from all four blades and predicted using the isolated rotor and rotor-fuselage models for the baseline case.

Figure 18. Blade tip deflections (flap, lead-lag and elastic torsion) measured from all four blades and predicted using the isolated rotor and rotor-fuselage models for the minimum noise case.

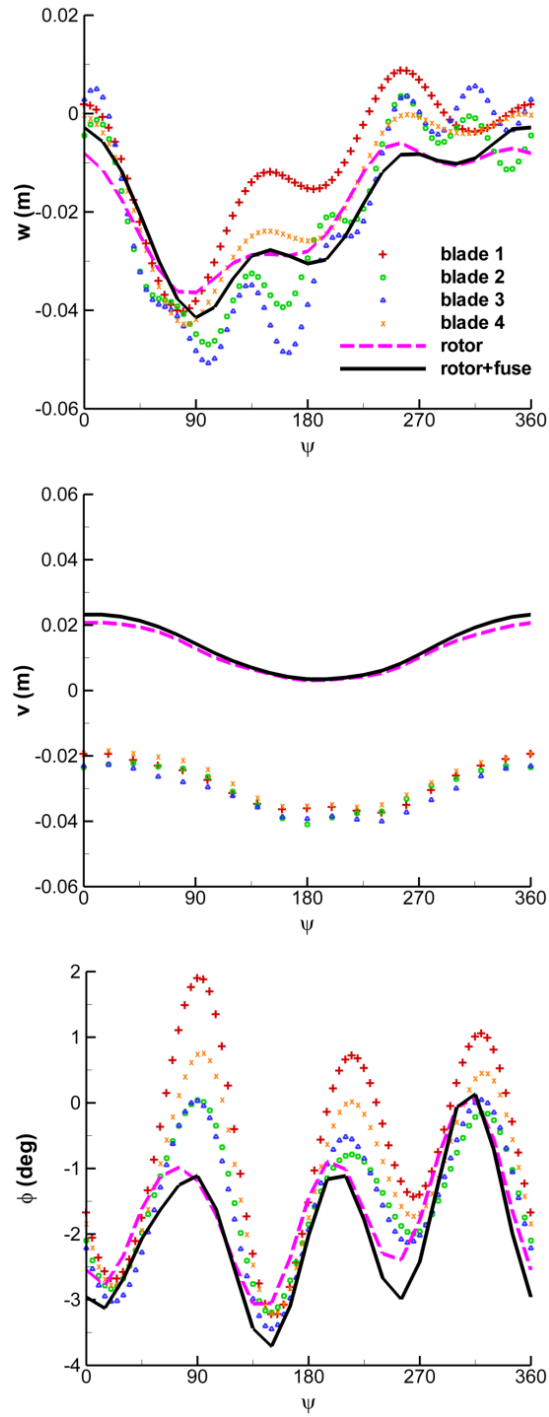


Figure 19. Blade tip deflections (flap, lead-lag and elastic torsion) measured from all four blades and predicted using the isolated rotor and rotor-fuselage models for the minimum vibration case.

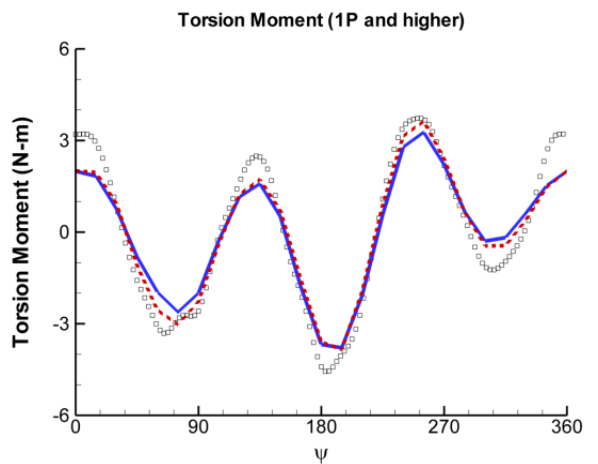
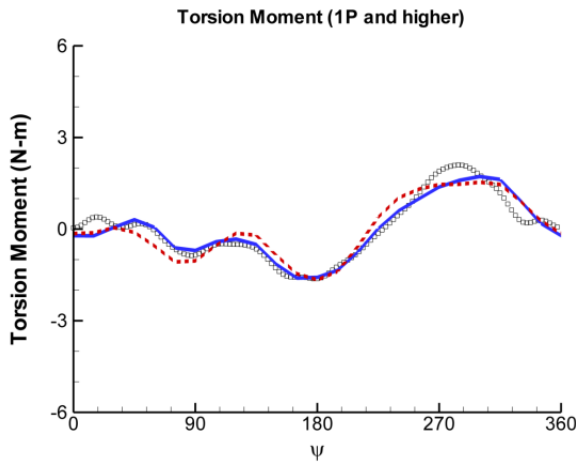
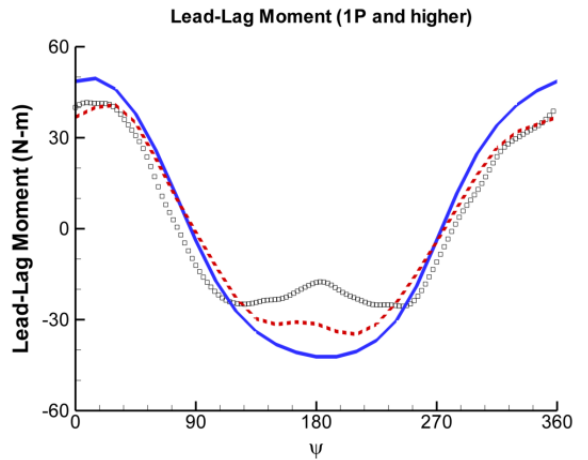
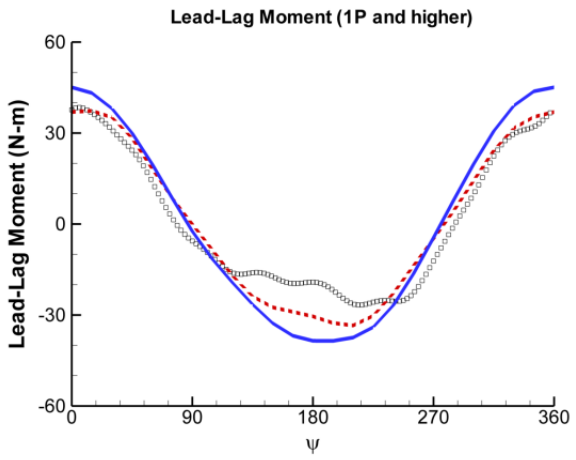
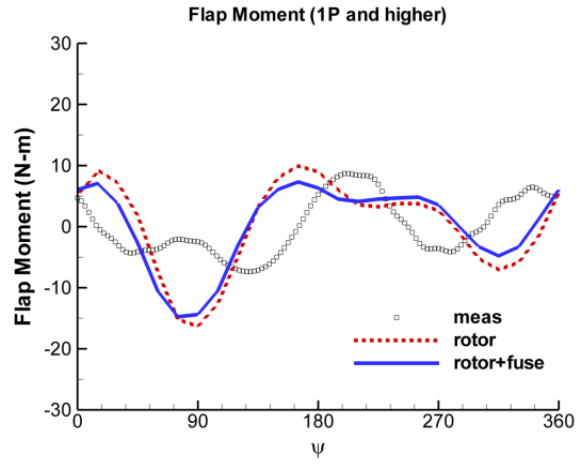
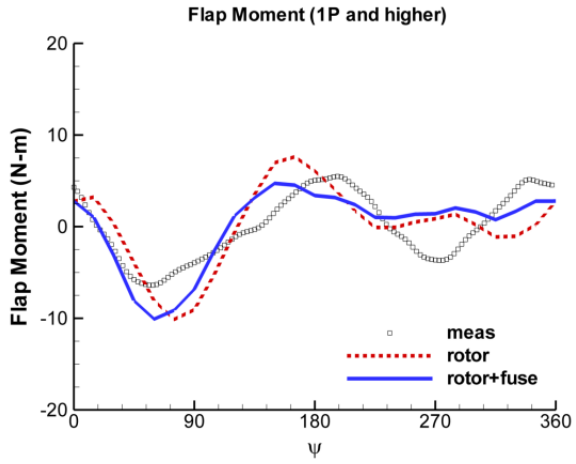


Figure 20. Oscillatory blade moments (flap and lead-lag at  $r/R=0.17$  and torsion at  $r/R=0.33$ ) using the isolated rotor and rotor-fuselage models in the baseline case.

Figure 21. Oscillatory blade moments (flap and lead-lag at  $r/R=0.17$  and torsion at  $r/R=0.33$ ) using the isolated rotor and rotor-fuselage models in the minimum noise case.

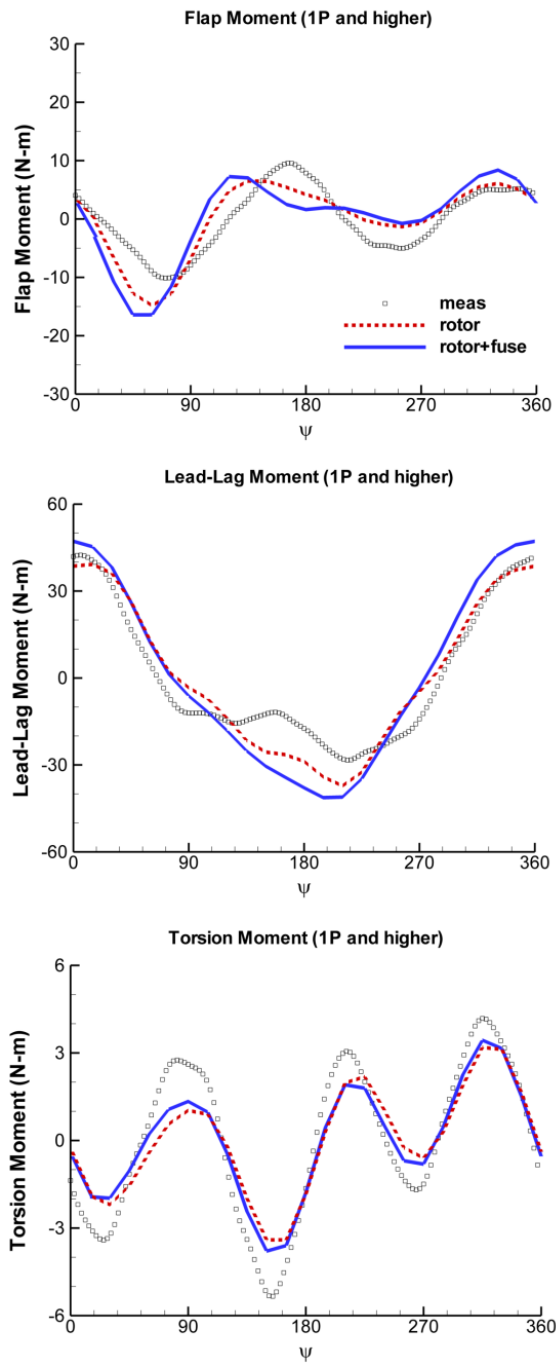


Figure 22. Oscillatory blade moments (flap and lead-lag at  $r/R=0.17$  and torsion at  $r/R=0.33$ ) using the isolated rotor and rotor-fuselage models in the minimum vibration case.

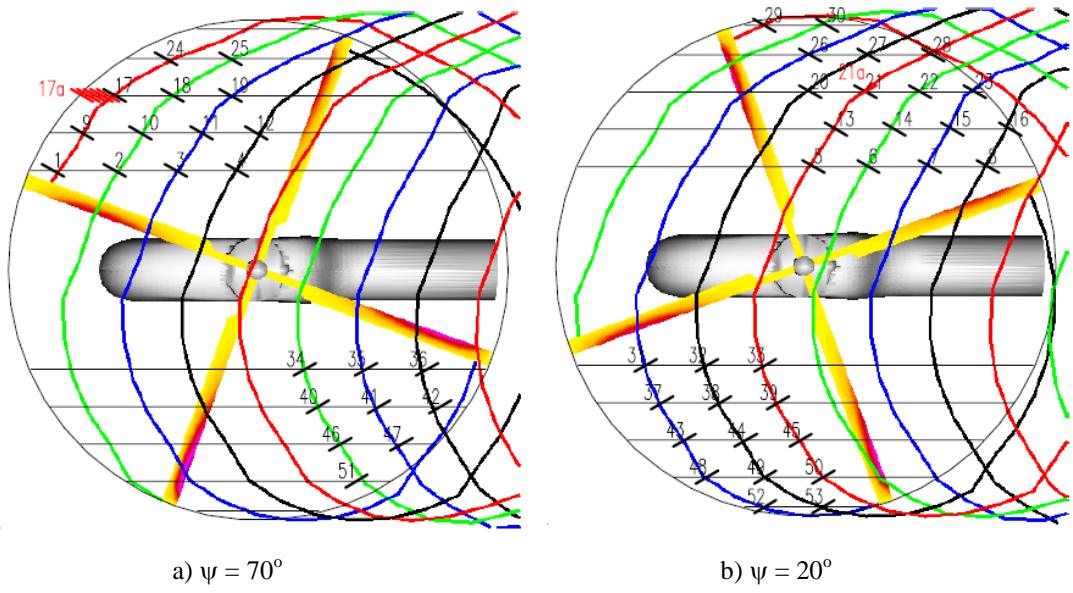


Figure 23. HART II PIV measurement plane positions in the baseline case [2].

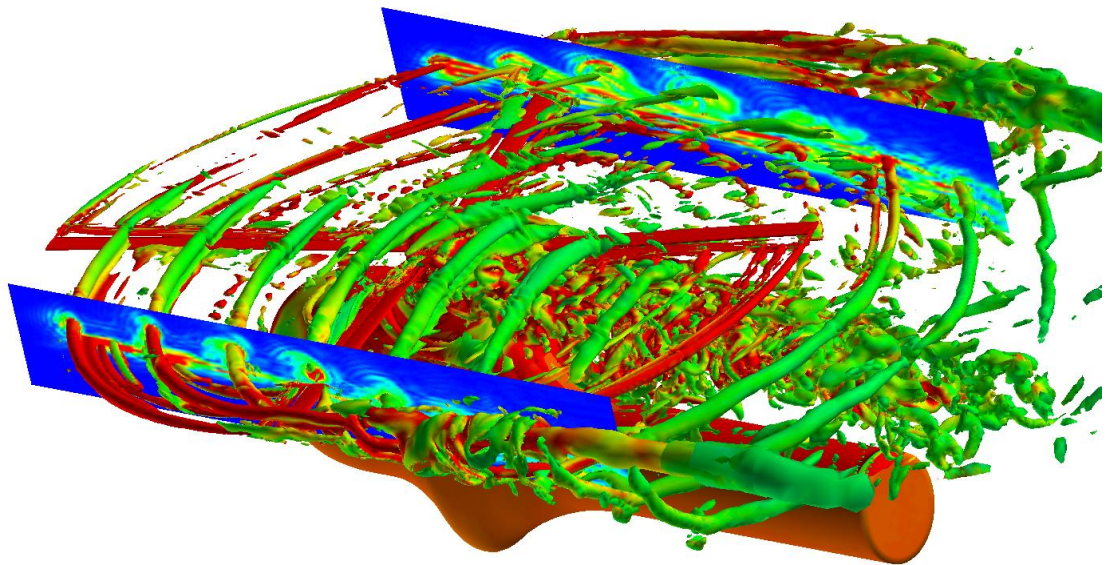


Figure 24. Rotor wake structure represented by the iso-surfaces of Q-criterion at  $20^\circ$  azimuth, colored by the vorticity magnitude with red indicating high in the baseline case.

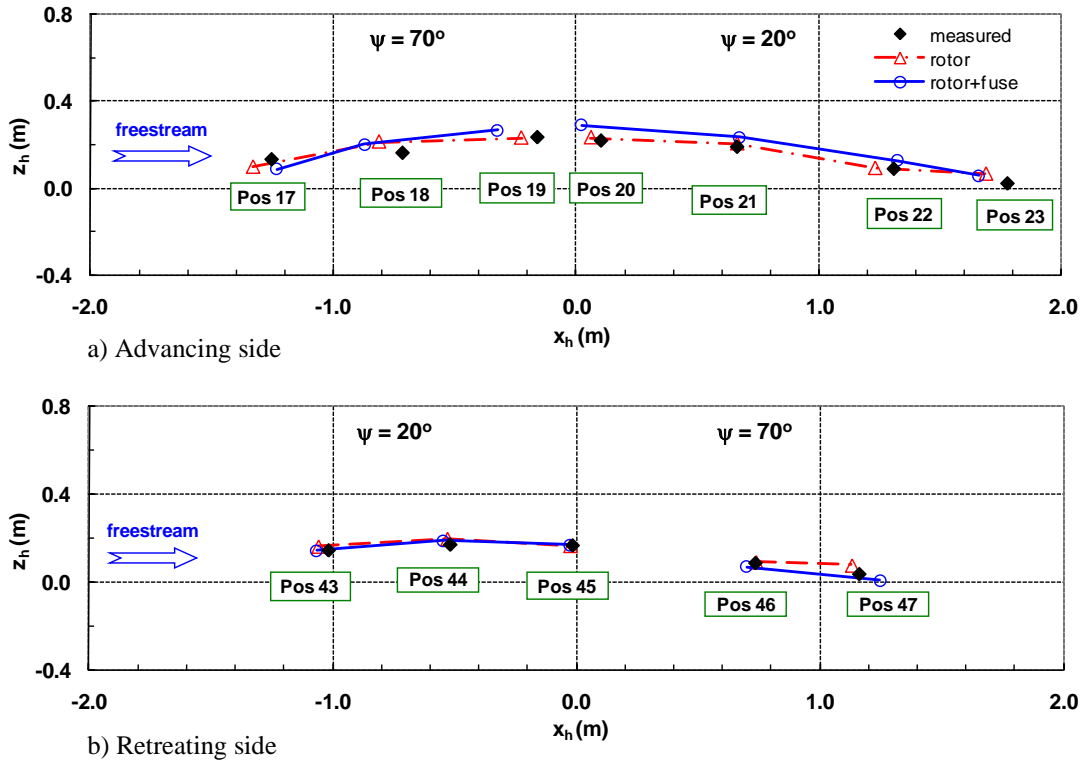


Figure 25. Comparison of the wake positions between the isolated rotor and rotor-fuselage models in the longitudinal cutting plane ( $y/R=\pm 0.7$ ) in the baseline case.

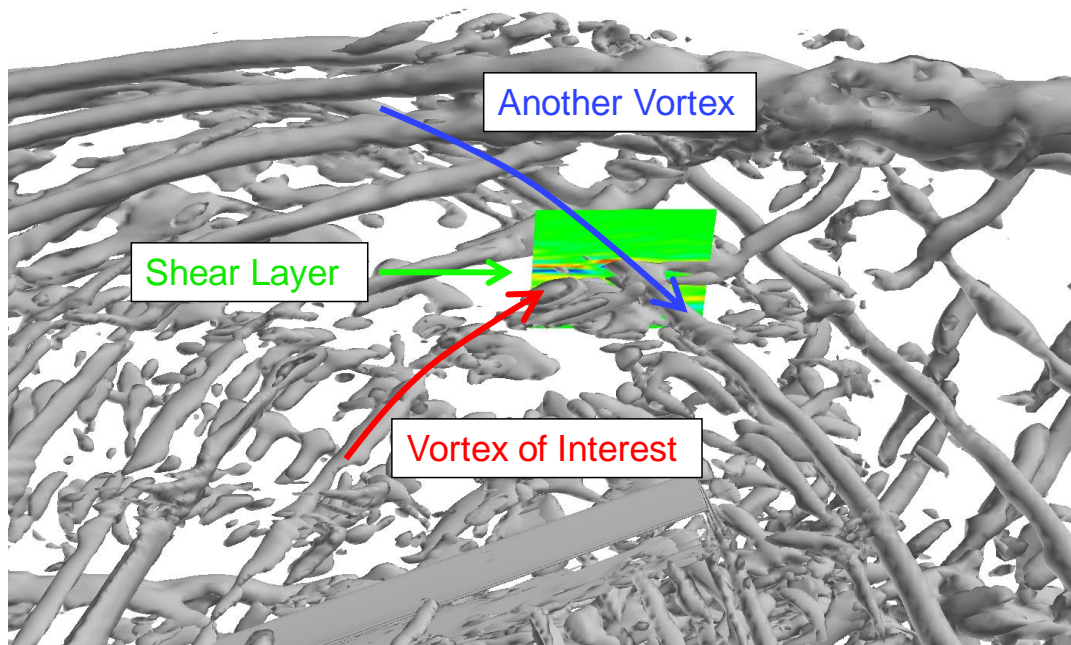
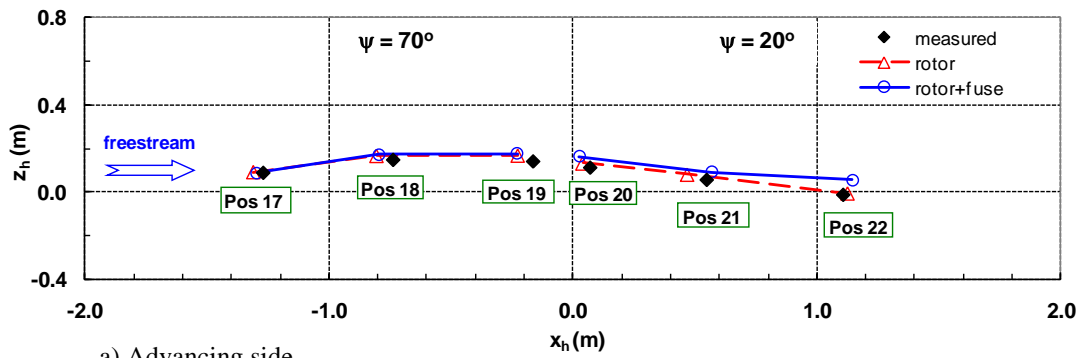
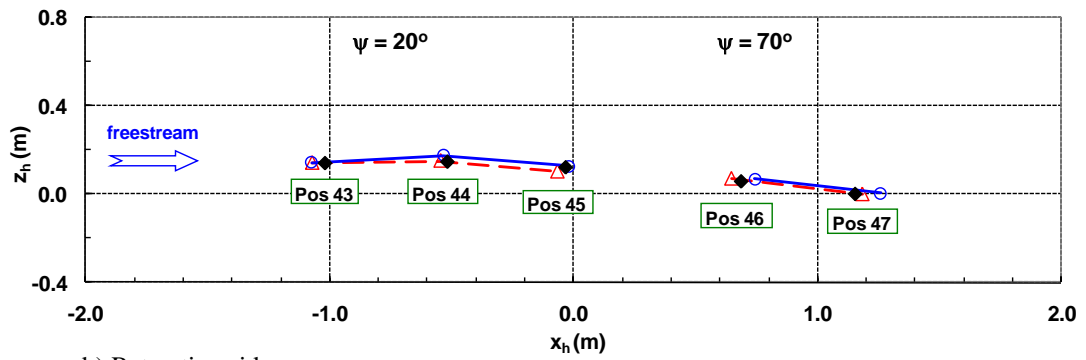


Figure 26. The detailed rotor wake structure adjacent to the PIV measurement position 23 in the baseline case, computed using the rotor-fuselage model.



a) Advancing side



b) Retreating side

Figure 27. Comparison of the wake positions between the isolated rotor and rotor-fuselage models in the longitudinal cutting plane ( $y/R = \pm 0.7$ ) in the minimum noise case.

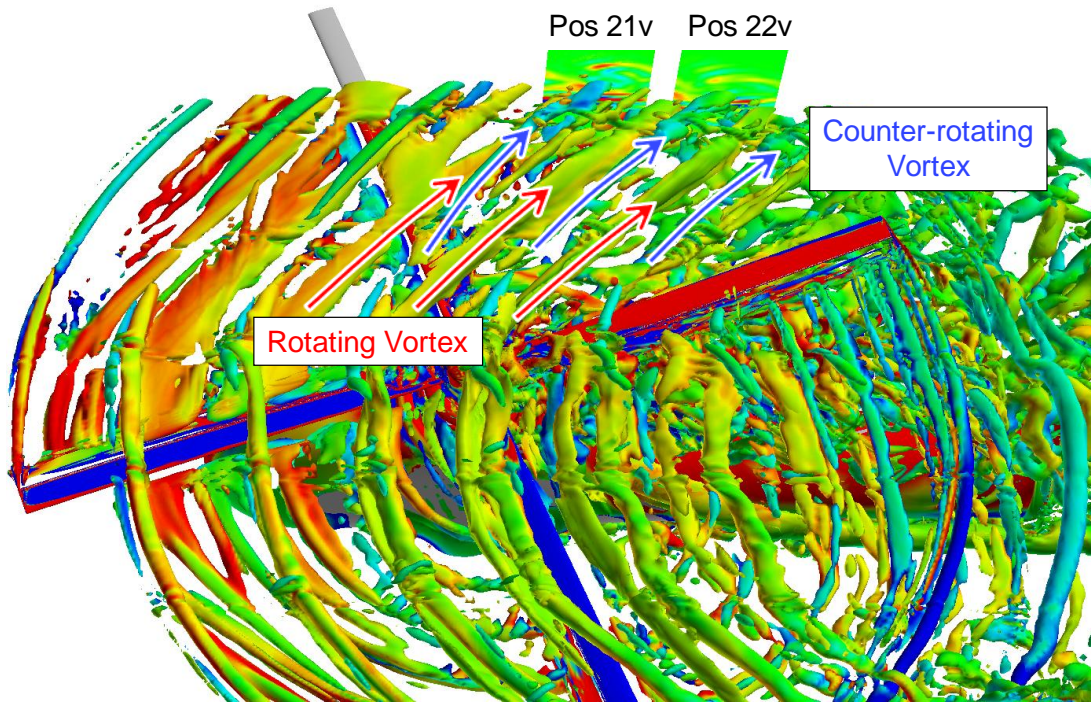


Figure 28. Rotor wake structure represented by the iso-surfaces of Q-criterion at an azimuth of  $20^\circ$  for the minimum vibration case, colored by the vorticity magnitude with red indicating high strength.

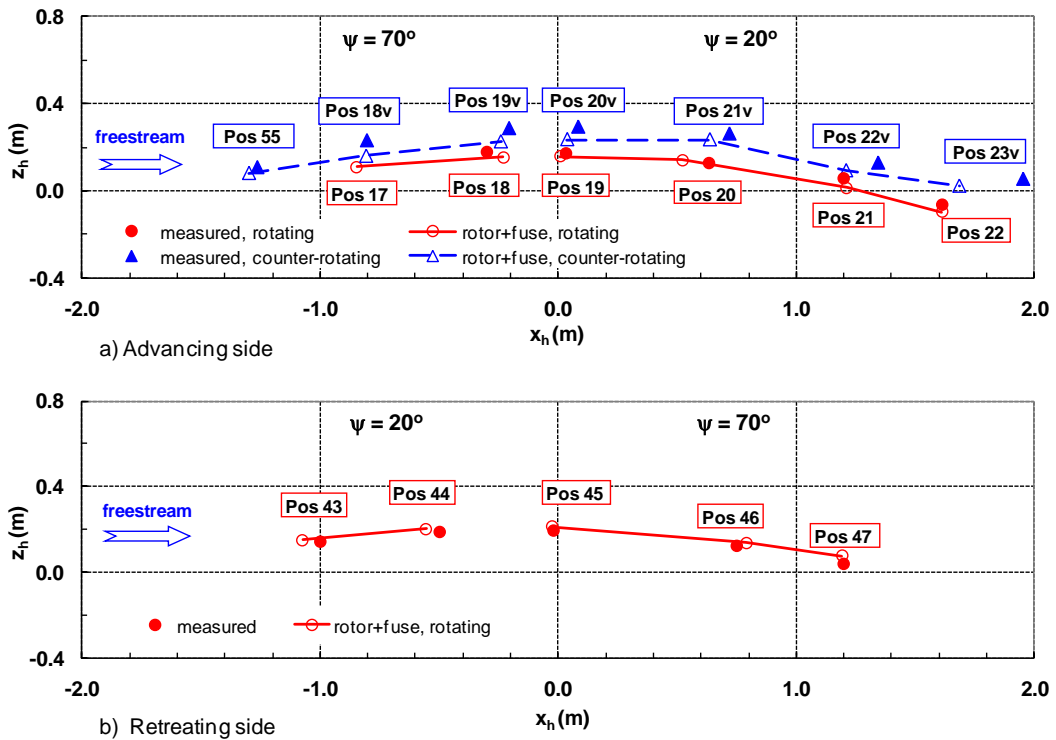


Figure 29. Comparison of the wake positions between the rotor-fuselage model in the longitudinal cutting plane ( $y/R=\pm 0.7$ ) in the minimum vibration case.